A SYSTEMATIC INVESTIGATION INTO β-PHASE TI-ALLOYS FOR BIOMEDICAL APPLICATIONS

L Melmoth

MPhil 2018

A SYSTEMATIC INVESTIGATION INTO β-PHASE TI-ALLOYS FOR BIOMEDICAL APPLICATIONS

By

LUCIE MELMOTH

A THESIS SUBMITTED IN PARTIAL FULFILMENT
OF THE REQUIREMENTS
OF MANCHESTER METROPOLITAN UNIVERSITY
FOR THE DEGREE OF MASTER OF PHILOSOPHY

Faculty of Science and Engineering

School of Engineering

Manchester Metropolitan University

June, 2018

Acknowledgements

I would first like to acknowledge my Director of Studies, Dr Lisa Simmons and the other members of my supervisory team, Prof Peter Kelly, Dr Marina Ratova and Dr Araida Hidalgo-Bastida of the Faculty of Science and Engineering at Manchester Metropolitan University. I am especially grateful for their constant guidance and encouragement.

I would also like to thank Dr Gary Miller, Miss Hayley Andrews and all other members of the technical support team at Manchester Metropolitan University, I am gratefully indebted for their help and support throughout my degree.

Furthermore, I would like to thank all of the postgraduate research students at Manchester Metropolitan University for their friendship and assistance. Special acknowledgements to Claire Mur'Tala, Sam Capp and Elisa Serra for their valuable support throughout my time at Manchester Metropolitan University.

Finally, I must express my very profound gratitude to my parents, Robin and Ann Melmoth, and to my partner, Carl Mcgovern, for providing me with unfailing support and continuous encouragement throughout my studies and through the process of researching and writing this thesis. This accomplishment would not have been possible without them.

Thank you.

Abstract

Total hip replacement procedures are becoming increasingly common and often necessary due to injury in young patients. The materials currently utilised have a relatively short lifespan in comparison with the growing life expectancy of the population; this inherently results in the requirement of revision surgery continuing to rise. It is therefore imperative to develop a more suitable material, with greater durability and biological tolerance to reduce the number of complex, disruptive, and ultimately costly revision procedures.

Currently, Ti-6Al-4V monopolises the metallic implant market; it has more desirable mechanical properties, including a relatively low elastic modulus (≈ 115GPa) and superior specific strength when compared to the cobalt-chromium and stainless steel alloys. However, in comparison to bone (≈ 30GPa) the elastic modulus is still too high. This leads to the bone remodelling, as a result of a changing stress/strain imposed, known as stress shielding; which could eventually lead to implant failure. In addition, efforts must be made to eliminate elements that have been associated with adverse reactions from the implant material. Recently, β-phase titanium alloys have shown promise; they have lower elastic modulus, more comparable to that of bone, than alloys in the α-β phase (such as Ti-6Al-4V) and the majority of alloying elements (such as tantalum and niobium) are currently believed to be non-toxic and highly biocompatible.

Ultimately, the chosen biomaterial and implant design should possess all of the following attributes: excellent biocompatibility, high corrosion and wear resistance, suitable mechanical properties and osseo-integration.

This thesis details a systematic approach, employed to develop and test a range of binary, titanium alloys, with alloying elements, niobium and molybdenum. The alloys were prepared via magnetron sputtering, before characterization and testing using techniques such as: X-ray diffraction; scanning electron microscopy; and energy dispersive X-ray spectroscopy. The alloys biocompatibility was also assessed using human mesenchymal stem cells, with alamarBlue® assay and scanning electron microscopy. The results obtained in this thesis using human mesenchymal

stem cells, with alamarBlue® assay and scanning electron microscopy, suggested very little or no toxicity in binary Ti-Mo alloys with Mo content less than 25 at% and no toxicity in binary Ti-Nb alloys; therefore all the alloys investigated in this thesis show promise for biomedical applications with the exception of Ti-50Mo. The research completed in this thesis also suggests that this method of fabrication and analysis is a time, and cost efficient method that gives an initial indication of the most suitable alloy systems; it is important to note that the method proposed would not be employed to manufacture any part of the hip implant, its sole use is at the initial stage of alloy development.

Contents

List of Tables

List of Figures

List of Abbreviations

AC	Alternating Current
bcc	Body-Centered Cubic
CVD	Chemical Vapor Deposition
DC	Direct Current
DFT	Density Functional Theory
DMEM	Dulbecco's Modified Eagle's Medium
EDX	Energy Dispersive X-Ray Spectroscopy
GOF	Goodness of Fit
HAp	Hydroxyapatite
hcp	Hexagonal Close Packed
hMSC	Human Mesenchymal Stem Cell
MSCBM	Mesenchymal Stem Cell Basal Medium
PBS	Phosphate Buffered Saline
PVD	Physical Vapor Deposition
QCM-D	Quartz Crystal Microbalance with Dissipation Technique
SEM	Scanning Electron Microscopy
SLM	Selective Laser Melting
THA	Total Hip Arthroplasty
XPS	X-Ray Photoelectron Spectroscopy
XRD	X-Ray Diffraction

1. Introduction

Total hip replacement procedures are essential to reduce pain and increase mobility in patients with conditions such as osteoarthritis, rheumatoid arthritis, post-traumatic arthritis, and childhood hip disease. Furthermore, owing to the populations increasing lifespan, the necessity for total hip replacement procedures is growing and resulting from the prosthesis' relatively short lifespan, on average about 15 years, the demand for revision surgery is also rising. The current market growth rate for reconstruction of failed hard tissue remains at around 25%, with 70-80% of biomedical implants being made of metallic materials and the remainder comprising of predominantly ceramic and polymeric materials (Li et al., 2014).

Figure 1: A range of hip prosthesis, comprising of different materials and designs (Gavrilov, no date).

Metallic implants are largely made from one of the following: stainless steels; titanium and its alloy; or cobalt-chromium alloys. Titanium, Ti, has a number of desirable qualities such as high corrosion resistance, adequate mechanical properties, and excellent biocompatibility. These attributes can be further enhanced by the act of alloying Ti with various elements. Currently, Ti-6Al-4V monopolises the metallic implant market; however, it's relatively high Young's modulus, ≈ 115 GPa, in comparison with cortical bone, ≈ 30 GPa (Kopova et al., 2016), results in a mismatch in elasticity at the bone-metal interface; frequently

causing an effect known as stress shielding. Stress shielding is a phenomenon that causes reabsorption of the natural bone, due to the difference in stiffness between the implant material and natural bone, leading to the implant loosening (Rack and Qazi, 2006). The longevity of metallic prosthesis, in the body's environment, is affected considerably by the likelihood that the material will corrode and wear. The human body is a hostile environment and can therefore lead to the corrosion of metals, releasing metal debris, and consequently a biological response (Asri, 2017). Metal wear, of greatest significance with metal-on-metal implants, causes the release of debris and non-compatible metallic ions into the body, generating consequences such as: allergic and toxic reactions; inflammation; pain; implant loosening; and may ultimately lead to implant failure (Long and Rack, 1998). It has been established that metal debris and metallic ions can have an impact, both locally and systemically, within the body (Hallab and Jacobs, 2017). Efforts have since been made to reduce the toxicity of Ti-alloys, through the trailing of alternative alloying elements, for example, vanadium, V, was replaced with niobium, Nb, and iron, Fe, generating Ti-6Al-7Nb and Ti-5Al-2.5Fe (Semlitsch, 1987). Whilst these alloys have an improved biocompatibility, their Young's modulus, equal to 105 GPa and 110 GPa, respectively, was still relatively high in comparison to bone, around 30 GPa, although slightly more preferable to Ti-6Al-4V. As discussed in section 1.2.2, a relatively high Young's modulus leads to the stress shielding effect (Long and Rack, 1998). More recently, β-type Ti-alloys appear to have more promising properties than their predecessors, with some researchers suggesting Young's modulus values as low as 35 GPa, similar to that of bone. (Li et al., 2014). A considerable effort has been focused on reducing the stiffness of the materials used and consequently the stress shielding effect; concurrently, some researchers have concentrated on other aspects of the implant such as geometry, shape, porosity, and coatings of the femoral stem to resolve the inherent problems, whilst being cautious not to create others (Geetha et al., 2009).

This review will investigate the associated clinical problems that lead to revision surgery of a total hip replacement before summarizing the ongoing research to overcome these obstacles. The review will cover: the biological and mechanical

properties of the materials currently used; implant design and shape; and a detailed look at the alloys and alloying elements used, particularly Ti and its alloys.

1.1Structure of the Hip Joint and Total Hip Replacement

1.1.1 The Human Hip Joint

In human anatomy, the hip joint is the largest weight bearing joint, consisting of a synovial ball and socket arrangement (Arthritis Research UK, 2011). The rounded head of the femur joins to the acetabulum of the pelvis. Articular cartilage covers both the acetabulum and the head of the femur; the cartilage is thicker at places more susceptible to load. The primary function of the hip joint is to load bear; as a result, the joint incorporates several factors to increase stability. The head of the femur is almost entirely encompassed by the deep structure of the acetabulum, primarily to reduce dislocation. An increased depth of the acetabulum, due to a fibrocartilaginous collar, named the acetabular labrum, further improves the stability. Surrounding ligaments also contribute, creating a strong, thickened joint capsule. The anatomy of the hip joint is illustrated in Figure 2.

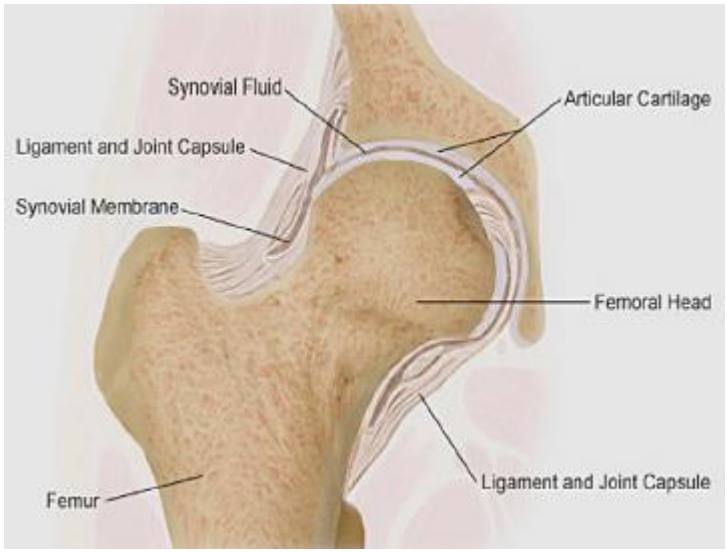

Figure 2: Anatomy of the human hip joint (Chen and Thouas, 2015)

1.1.2 Total Hip Replacement Geometry

A total hip prosthesis comprises primarily of three components: stem, head, and socket, replacing the femoral stem and head, and pelvic acetabulum, respectively.

Various combinations of materials are used for the different components, including, metallic alloys (head, stem and socket), polyethylene (lining of the socket) and ceramics (head and socket) (Chen and Thouas, 2015); a possible arrangement is depicted in Figure 3.

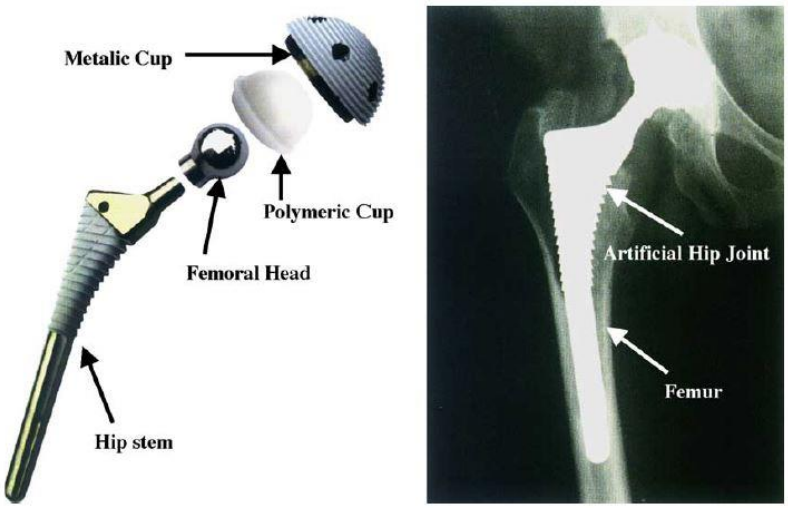

Figure 3: Schematic diagram of artificial hip joint (Liu et al., 2004)

1.1.3 Revision Surgery and its Causes

Total hip replacement procedures are becoming increasingly common, mainly due to conditions such as osteoarthritis and osteoporosis, but also as a result of trauma (Bourn, 2003). According to the National Joint Registry, the NHS performed 87,773 hip procedures in 2016 (*14th Annual Report*, 2017). In the first instance, a primary total hip replacement procedure is performed, where the arthritic or damaged joint is replaced with an artificial implant. However, over time the implant can fail, introducing the necessity for further procedures, commonly referred to as revision procedures or revision surgery (Arthritis Research UK, 2011). The clinical indications that contribute to implant failure and subsequent revision surgery include: aseptic loosening, the failure of a bond forming between the implant and natural bone, either initially or over time and without infection; pain, although sometimes a sole factor pain usually occurs alongside another indication; lysis, the loss of bone; adverse reactions to particulate debris, with metal-on-metal bearings having the highest incidence; and infection. Between 2009 and 2015, of the 57,162 single-stage revision procedures performed, 46% were attributed to aseptic loosening,

22% to pain, 14% to lysis, 12% to adverse soft tissue reactions to particulate debris, and 4% to infection (*13th Annual Report*, 2016). Unfortunately, the success rate of revision surgery is relatively low (Bozic et al, 2015; Geetha et al., 2009).

The National Joint Registry's 14th Annual Report states that, from the 890,681 recorded hip replacements over 13 years, the probability of revision after a primary hip replacement is 6.8% at 13 years, across all patients. The probability of revision increases for patients aged less than 55 years at the time of implantation, for female patients the probability is 13.5% at 13 years, and for male patients the probability is 10% at 13 years. Very low revision rates are seen for patients over the age of 75 at the time of implantation; their hip implant remaining unrevised across their remaining lifetime (14th Annual Report, 2017). There are several factors contributing to the rising number of primary and revision hip replacement procedures, these include the increasing longevity of the population and the lifespan of the materials used. Revision and re-revision surgery is particularly complex due to complications encountered during removal alongside the initial requirement for revision.

1.2Implant Design and Contributing Factors

This section will focus on the properties an implant must possess to succeed within its role; alongside reviewing the variety of ways that researchers and clinicians have developed new ideas, techniques and materials.

1.2.1 Biocompatibility

Biocompatibility was first defined as a non-living material's compatibility with the body, thus causing no unnecessary harm to the patient (Long and Rack, 1998); granting this continues to be the primary definition, it is now apparent that not only should the material reside harmoniously in the body, it should also be appropriate for the application intended (Park and Lakes, 2010; Williams, 2008).

Hip prosthesis, like any foreign object in the body, may stimulate an auto-immune response, reducing the likelihood of the implants success (Ridzwan et al., 2007). Correspondingly, to excel in its role, an implant material must cooperate fully with

the human body's normal functions, without causing any inflammatory or allergic reactions. There is continuing clinical concern regarding the release of chemically active metal ions, which bind to proteins and remain in a solution form and then disseminate systemically into surrounding tissues, bloodstream, and remote organs. Some historical research has suggested that V causes adverse tissue reactions and aluminium, Al, has been associated with potential neurological disorders (Bondy, 2010; Crapper McLachlan, 1989; Silva et al., 2004). However, the quantity of metallic ions released from a hip implant may depend upon factors such as, alloy composition, design and production techniques, the individual's lifespan, usage, and specific loading. Hallab and Jacobs state the relevance of the quantity of metallic ions with regards to toxicity and its effect on the body. They suggest that the levels of metals released from implant degradation are unlikely to be excessively high and that the association of metal release from orthopaedic implants with any associated toxicity is conjectural since cause and effect have not been established, yet (Hallab and Jacobs, 2017).

Researchers have speculated that a variety of elements, such as Ti, zirconium, Zr, tantalum, Ta, platinum, Pt, Nb, silver, Ag, gold, Au, molybdenum, Mo, Al, and Fe are biocompatible, produce no adverse tissue reactions, and are not cytotoxic (Geetha et al., 2001; Liang et al., 2016). Although the results found in these studies may support the evidence of a biocompatible nature of such elements, it should not be hypothesised that the same result would be observed for all variables. Li *et al* compared the cytotoxicity of several elements using a human osteosarcoma cell line, $SaOS_2$, and found some contrasting results when comparing bulk and powder forms of the same element. Other variables including: the environment, be it temperature, pH level, oxygen level or surrounding fluid; the type of molecule; and the length of exposure time, may also have a bearing on cytotoxicity and biocompatibility (Sullivan et al, 2006). In conclusion, predicting how a specific alloy composition will behave within its role as a hip implant, based on its elemental components, is challenging without extensive *in vivo* testing. At present, initial *in vitro* testing of implant materials is the most reliable method of reducing the likelihood of an implant material causing a reaction within the human body.

Researchers use many different cell lines, dependent on the position and desired use of the implant, to perform this testing. The following sub-sections detail cell culture techniques, the assays used, and some common cell lines.

1.2.1.1 *Cell Culture*

Cell culture, or tissue culture, is the technique of growing cells outside of the body. The cells, placed either in tubes, dishes or flasks, spontaneously proliferate in the presence of artificial media, containing the necessary nutrients, and desirable conditions, such as 37°C and 5% carbon dioxide, to form a monolayer or suspension. Depending on the cell type, the ideal surface coverage is said to be 80-90% confluence. Once at 100% confluence, contact inhibition alters the cells gene expression, cell shape, activity, and cell surface markers (Harrison and Rae, 1997). At this stage, the cells are subcultured by transferring them to a new vessel, or passaged by liberation, using an enzyme, trypsin-EDTA, enabling their continued growth and encouraging larger cell numbers. Unfortunately, amid cell culture there is a risk of genetic or epigenetic alteration; if the mutation grants the cell a small advantage in growth rate there is a possibility the abnormal, culture-adapted cell, could overgrow the rest of the culture and as a consequence, represents the culture en masse. This inevitably produces cells with different properties to those found *in vivo*, described as artefacts of cell culture (Slack, 2012). As a result of this phenomenon, the number of passages should be kept to a minimum to ensure reliable experimental results.

1.2.1.2 *alamarBlue® assay*

alamarBlue® is the trademark name for resazurin, used for the analysis of cell proliferation and viability. Cell viability refers to the measure of cells that are living and capable of developing and reproducing, thus making them suitable for use in experiments. The technique consists of exposing cells to the weakly fluorescent blue dye, resazurin. Upon entering the viable cells, the non-toxic, permeable dye is continuously reduced to resorufin (pink in colour and highly fluorescent). The evident change in colour is easily measurable by colourimetric or fluorometric

reading, generating a quantitative measure of proliferation and viability (Al-Nasiry *et al*., 2007), that is directly proportional to cell number.

1.2.1.3 *Other Biological Techniques*

The formation of bone comprises a complex set of events, beginning with the recruitment and proliferation of osteoprogenitors, a cell type with the capacity to form bone, followed by cell differentiation, osteoid formation and finally mineralisation (Ogura *et al*., 2004). When human mesenchymal stem cells, hMSCs, are cultured *in vitro,* using osteogenic media, culture media such as DMEM or MSCBM supplemented with 10% fetal bovine serum, 1% penicillin/streptomycin, 200 µM ascorbic acid, and 0.1 µM dexamethasone, and 10 mM b-glycerophosphate, the described stages usually occur within 28days (Li *et al*., 2017). Alizarin Red S Staining assay can be used to quantify the extent of osteogenic differentiation, through the bonding of Alizarin Red S and calcium, deposited during mineralisation, producing a bright red stain (Birmingham *et al*., 2012).

1.2.1.4 *NIH 3T3s*

In the early 1960's, Howard Green and George Todaro isolated, from a mouse embryo, fibroblast cells. The cells grown in Petri dishes were passaged every three days irrespective of confluence. Green and Todaro named the series of cells as a reference to this rigorous three day strategy, 3T3, 3T6 and 3T12, where '3T' stood for the three day transfer and the final digit described the number of cells plated to the nearest one hundred thousand. The 3T3 cells displayed an established cell line, proliferating in a single monolayer, whilst never reaching confluence. The cells plated as 3T6 and 3T12 proliferated unpredictably with a visual resemblance to tumours (Todaro and Green, 1963).

More recently, for biomaterial research purposes, NIH 3T3 cells have been predominantly used to assess cell adhesion. Other testing such as cytotoxicity and adverse tissue reactions would not provide valid data for the application of biomaterials in humans. Giannini *et al* utilised NIH 3T3 cell's fibroblast nature, to investigate a material's potential to reduce cell adhesion and proliferation of specific cell types. The aim of the study was to overcome or delay the

uncontrollable proliferation of fibroblast cells, due to evidence that this behaviour causes a fibrous encapsulation of the implant, ultimately leading to implant failure (Giannini *et al*., 2014). Lord *et al* also employed NIH 3T3 cells for cell adhesion purposes, to investigate the potential of the quartz crystal microbalance with dissipation technique, QCM-D, to identify the spreading and initial adhesion of cells in contact with biocompatible surfaces pre-coated with proteins (Lord *et al*., 2006).

1.2.1.5 *Stem Cells and Human Mesenchymal Stem Cells*

Stem cells form the foundation of every organ and tissue in the body. They have two distinguishing features in comparison to other cell types; the capability to self-renew, producing more cells like them, and the ability to differentiate toward two or more mature cell types, defined as multipotent (Karp, 2014). Multipotent cells, such as hMSCs, are a limited type of pluripotent cell (Zhang *et al*., 2011), where pluripotent cells have the capacity to form any of the cell types found in the normal body (Slack, 2012).

Isolation of stem cells is possible from tissues that differ in both development, i.e. fetal or adult, and in anatomy. hMSCs, are a form of adult stem cell; predominantly isolated from bone marrow, whilst also found in other tissues including adipose, amniotic fluid and membrane, peripheral blood, and skeletal muscle (Ullah *et al*., 2015); they have applications in tissue engineering and regenerative medicine (Quiroz *et al*., 2008). Bone marrow-derived hMSCs, accepted as the standard for comparison with hMSCs taken from other sources, require an invasive procedure for isolation (Zhang *et al*., 2011). Studies have shown that cell culture duration and an increasing number of passages impacts on hMSC morphology, viability and their ability to differentiate declines as the cells begin to senesce (Eggenhofer *et al*., 2014; X. Wei *et al*., 2013). Sawyer *et al* utilised hMSC's capacity to differentiate into osteoblasts to mimic the *in vivo* environment, stimulating a specific cellular response such as bone regeneration (Sawyer *et al*., 2007).

1.2.2 Mechanical Properties

The mechanical properties of most importance are an adequate mechanical strength, needed to tolerate the mechanical loading caused by the human body, and a suitable Young's modulus, needed to reduce the phenomenon known as stress shielding (Lopes *et al*., 2015). As the name suggests, stress shielding is the shielding of the bone from the load by the implant material, caused by the difference in mechanical properties resulting in a lack of even distribution of force. Bone has a natural ability to develop a structure most suited to accommodate the forces acting upon it. According to Wolff's Law, areas of bone experiencing decreased levels of load or stress will respond by decreasing bone mass; bone will remodel with the changing stress or strain imposed on it (Wang, 2003). This observation is known as bone reabsorption (Park and Lakes, 2010). Yan *et al* showed a correlation between bone loss around the implant and the value of the Young's modulus of the implant (Yan et al., 2011). The more similar the elastic properties of the implant material to bone, the more evenly distributed throughout the new assembly the loads applied would be. The even distribution of the loads applied means the bone would be subjected to stresses within normal levels, encouraging the bone to behave more normally and decreasing the occurrence of bone reabsorption and ultimately the stress shielding effect.

The Young's modulus of a material is a measure of the materials stiffness within the elastic region of deformation. A stress-strain curve for Ti-6Al-4V at room temperature is depicted in Figure 4; the significant change in the graphs curve illustrates the limit of proportionality, at which point the material undergoes permanent deformation.

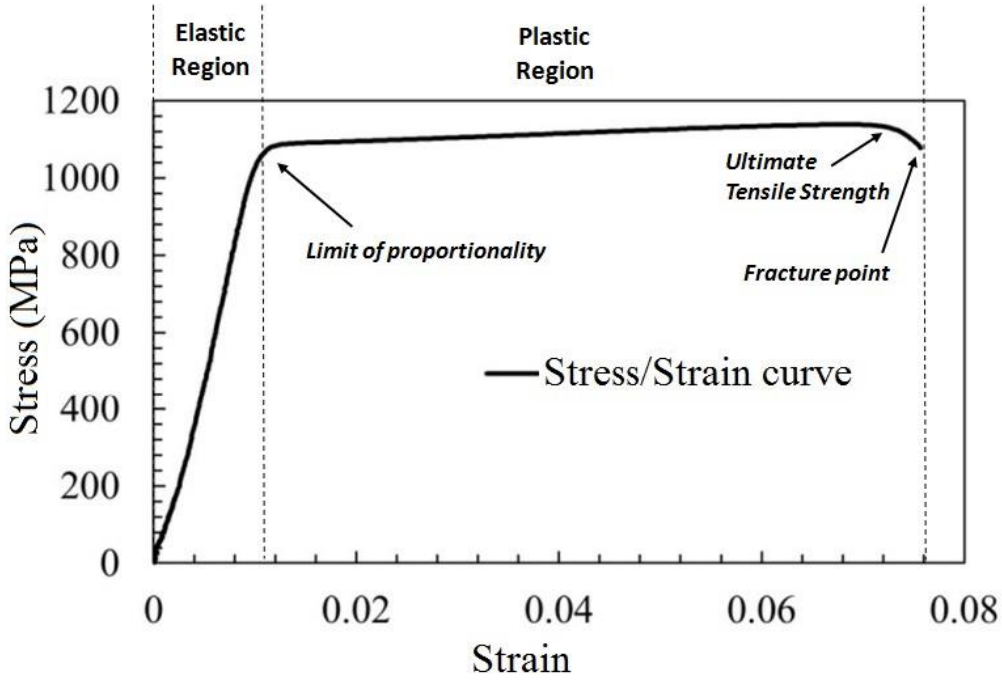

Figure 4: Stress–strain curve for Ti6Al4V at room temperature. Adapted from Anjum et al (Anjum et al., 2015)

Young's modulus, E, is the ratio of stress, σ, to strain, ε, where σ is the force, F, per unit cross-sectional area, A, and ε is the change in length, ΔL, as a function of the original length, L .

$$E = \frac{\sigma}{\varepsilon} = \frac{FL}{A\Delta L} \tag{1}$$

Tensile strength is the maximum stress that a material can withstand before failing; for most Ti-alloys it is related to Young's modulus and both tend to decrease simultaneously. This can be problematic when reducing the Young's modulus to a suitable level, the tensile strength may become inadequate, leading to the implant fracturing and failing. Huggler *et al* recommend the minimum ultimate tensile strength to be 90 $Kpmm^{-2}$ (equivalent to ≈ 883 MPa) (Huggler and Weidmann, 1976). However, the successful current use of alloys, with lower ultimate tensile strength, dispels their suggestion (Chen and Thouas, 2015). Cortical bone and cancellous bone have tensile strength values of 100-230 MPa and 2-12 MPa,

respectively, in contrast to the alloy, Ti-6Al-4V, which has a relatively high tensile strength of 860 MPa (Hermawan *et al*., 2011; Kokubo *et al*., 2003).

Design and development of implant materials must also take into consideration fatigue strength, where initially sheer stress causes the nucleation of a micro-slip within a grain. This occurrence is commonly irreversible due to the formation of an initial micro-crack which inherently oxidises; under further repeated tensile loading the micro-crack grows to a critical size crack; the problem is no longer a surface phenomenon. Once the crack is of the macro scale it grows rapidly, finally resulting in complete failure. Surface imperfections, corrosion, and wear all increase the likelihood of a slip nucleating. α-β Ti-alloys have higher fatigue strength than 316L stainless steels, and comparable fatigue strength to cobalt-chromium alloys. However, the uniformity within the micro-structure of β Ti-alloys results in less satisfactory fatigue strength when comparing to α-β Ti-alloys; Chen *et al* discuss possible solutions (Chen and Thouas, 2015). Ti-alloy phases will be further discussed in section 1.3. Ti's lower modulus and superior specific strength (strength/density) when compared to stainless steels and cobalt-chromium alloys has presented it as a suitable base for an alloy system to be developed.

1.2.3 Osseo-Integration

Recently, researchers have started to explore the biological response of Ti-alloys with particular interest in the alloy's bioactive nature and osseo-integration. Osseo-integration, derived from the Latin words "*os*" meaning bone and "*integrare*" meaning make whole, is the capacity for the implant to integrate with the adjacent bone and other tissues (Goriainov *et al*., 2014). Micromotions occur when an implant does not bond with adjacent bone, this results in the formation of fibrous tissue around the implant leading to loosening of the prosthesis. Chen *et al* suggest that surgeons in clinical practice have recently documented intimate integration of Ti with host bone tissue, contrary to prior thinking that metallic biomaterials, although bio-inert, rarely encourage bone growth and integration in a bioactive nature (Chen and Thouas, 2015).

Chen *et al* also suggests that without prior coating, a carbonated hydroxyapatite layer forms on the surface, before the collagen fibres of the host bone adhere to the carbonated apatite layer (Chen and Thouas, 2015). Researchers have attempted to accelerate this process by the adoption of various surface treatments and coatings, such as hydroxyapatite, employed to improve the alloys ability to form a strong bond with the living bone (Satoh *et al*., 2013). Hydroxyapatite, a calcium phosphate, with chemical formula [$Ca_{10}(PO_4)_6(OH)_2$, HAp] (Oliveira *et al*., 2016; Heimann, 2006), belongs to the mineral family known as biological apatites. It naturally occurs as the predominant inorganic component in mammalian teeth and bones (Wei *et al*., 2016). HAp has a bioactive nature, as a direct result of its chemical composition, containing ions commonly found in the physiological environment (such as Ca^{2+}, K^{+}, Mg^{2+}, Na^{+}, etc.) (Wang, 2003). A bioactive material is one that encourages a biological response at the tissue/material interface, which results in a bond between the material and the tissue (Cao and Hench, 1996). Mohseni *et al* have compiled both qualitative and quantitative data for a number of different HAp coating techniques: plasma spray depositing, hot isostatic pressing, thermal spray, dip coating, pulsed laser deposition, electrophoretic deposition, sol-gel, ion beam assisted deposition, and sputtering. Their findings conclude that the best adhesion of HAp coating on Ti-6Al-4V substrate is obtained by the sputtering technique with an adhesion strength of 80 MPa; pulsed laser deposition at 1000 laser pulses had the lowest bonding strength with adhesion strength < 10 MPa (Mohseni *et al*., 2014).

1.2.4 Implant Geometry and Shape

As an alternative to developing new biomaterials, some studies have investigated the prospect of varying the shape, size or porosity of the implant to obtain more suitable biological and mechanical properties.

Statistics, published by the National Joint Registry, show that the femoral head size has a significant impact on the number of revision surgery procedures. However, statistically the most suitable size is dependent on the material combination used and the recipient's physical characteristics and activity levels. High rates of

dislocation, leading to revision surgery, have been noted in cases involving small femoral head size for the majority of material combinations (Ng et al, 2011). However, for metal on metal implants, a larger head size, which has been noted to reduce the number of dislocations, also increases the contact area between the cup and ball, leading to higher revision rates caused by adverse reactions to particulate wear debris (*13th Annual Report*, 2016; *15th Annual Report,* 2018). This occurrence can be described as a greater volumetric wear but may be counterintuitive because the pressure per unit area would be reduced for a larger contact area; the lubrication and sealing of the joint may also contribute to the amount of wear, the production of particulate debris and its diffusion into the rest of the human body.

Recently, research into porous implants has shown promise, particularly through the improvement of porous implants' elastic modulus and potential for osseo-integration, in comparison to historically produced solid implants. Yan *et al* employed a strain magnitude based bone remodelling theory to investigate the effect of the implant material and porosity on the bone remodelling, evaluated by analysing the loss of bone density. Solid cobalt–chrome, solid Ti and porous Ti, with different porosities, were considered and the authors concluded that bone loss around the implant is clearly linked to the value of the elastic modulus, the value of which can be altered by porosity (Yan *et al*., 2011).

Jones *et al* have developed a process, using Selective Laser Melting, SLM, that incorporates a laser which melts precisely arranged powder in consecutive layers, either elemental or alloyed, to produce a three dimensional, mixed porous and solid object (Jones, 2006). This manufacturing technique has been developed to enable the production of implants with appropriate porosity in an infinite variety of shapes and sizes. Previous research suggested that pore size, beneficial to encourage bone in-growth and therefore most effective for implants, is in the range 100 to 700 µm. Bone in-growth has been shown to increase with porosity. However, in order to ensure the mechanical properties of the implant do not become inadequate, the overall porosity should not exceed 80% (Bobyn *et al*, 1980; Kienapfel *et al*, 1999; Mullen, 2009). Evans *et al* describe the analysis of variability in the SLM technique, highlighting the importance of repeatability for implant

success. Previous techniques, such as plasma spraying and sintering, were not able to provide the same level of consistent accuracy required for mass production, to ensure the implant performs as its porous design intends (Evans, 2017). Simoneau *et al* have also used an SLM technique to manufacture a porous stem and dense stem replica to determine an optimum porosity by exploring the relationship between the bone ingrowth requirements and the manufacturing technology limitations. The limitations to the manufacturing method resulted in around a 10% porosity increase than predicted in the porous stem. The authors concluded that there is a better match between porous implant stiffness, with that of bone, while still providing adequate mechanical properties at the porosity investigated. They propose that future work will be devoted to the biomechanical *in-vitro* testing of artificial femurs implanted with both the porous and dense stems, to evaluate the reduction of stress shielding (Simoneau *et al*., 2017).

It is reasonable to conclude that many factors including material, shape and size, all have an impact on whether an implant will be successful. The alloy-system used to manufacture porous implants is still of importance and biocompatibility of the materials must be carefully considered in order to tackle the inherent problems with metallic wear debris. However; porous implants appear to offer advantages, including reduction in the stress-shielding effect, and efficient use of material and subsequently reduced implant weight.

1.3Titanium and its Alloys

An alloy consists of two or more metallic elements, predominantly produced to enhance and improve the properties of the pure metal. At ambient temperature and pressure, pure Ti has a hexagonal close packed, hcp, α phase crystalline structure; when heated above 882°C the crystal structure undergoes an allotropic transformation to body-centred cubic, bcc, β phase (Trinkle, 2003). Depending on their room temperature microstructure, Ti-alloys can be classified as either α, near-α, α + β, metastable β or stable β (Long and Rack, 1998). Elements, when alloyed with Ti, can be categorised by their effect on the stabilities of the α and β phases. Hence, Al, oxygen, O, nitrogen, N, and gallium, Ga, are all α-stabilisers, whilst Mo,

Nb, V, tungsten, W, and Ta are all β-stabilisers; Zr, tin, Sn, and silicon, Si, are considered neutral elements. V, Nb, Ta, and Mo are isomorphic to β-Ti and form a substitutional solid solution (Baker, 1992; Kolli and Devaraj, 2018).

Currently, Ti-6Al-4V is the most commonly used Ti-alloy system in total hip arthroplasty, THA. Its α-β phase structure contributes to its high Young's modulus of ≈ 115 GPa and tensile strength of 860 MPa in comparison with cortical bone and cancellous bone, 7-30 GPa, 100-230 MPa and 0.05-0.5 GPa, 2-12 MPa, respectively (Hermawan *et al*., 2011; Kokubo *et al*., 2003). More recently, β-phase Ti-alloys have been shown to have more comparable Young's modulus and improved biocompatibility. Liang *et al* have recently developed a new β-phase Ti alloy system, Ti-31Nb-6Zr-5Mo, with a low Young's modulus of 44 GPa, whilst still maintaining a respectable tensile strength over 700 MPa (Liang *et al*., 2016). Matsumoto and co-authors report that the Ti-alloy system, Ti-35Nb-4Sn has the lowest elastic modulus of 42 GPa (Matsumoto *et al*., 2005). Other β-Ti alloy systems, partially researched include Ti-25Nb-6.25Zr and Ti-25Nb with calculated Young's moduli of ≈ 50 GPa and ≈ 80 GPa, respectively (Karre *et al*., 2015), six alloy stoichiometries, in the Ti–Nb–Zr alloy system, with the lowest Young's modulus ≈ 38.8 GPa (You and Song, 2012) and Ti-35Nb-4Sn-6Mo-9Zr with Young's modulus ≈ 65 GPa (Dai *et al*., 2013). The aforementioned studies present some rationale behind the chosen alloying elements, but lack justification of the number of elements chosen and the ratio of alloy compositions used.

1.3.1 Alloying Elements

In recent years, the majority of research has focused on the mechanical and biological properties of binary, ternary and quaternary β-phase Ti-alloys. A wide variety of alloying elements and compositions has been investigated, however, there is yet to be a systematic review of the function that alloying elements have. The most commonly chosen alloying elements, Nb, Mo, Ta, and Zr, will be reviewed with respect to the rationale for their use.

1.3.1.1 *Niobium, Nb*

The element Nb, a typical β-stabilizer, is beneficial to Ti-alloy systems as a result of its bcc structure, similar atomic radius, solid solution, and no biological toxicity (Liang *et al*., 2016); although, there is an added complexity when analysing the structure of a solid solution, using X-ray diffraction, XRD, due to the difficulty in distinguishing between two elements within the same crystalline structure. The phase diagram, shown in Figure 5, illustrates an isomorphous binary Ti-Nb alloy, above the β transus temperature of pure Ti, 882 °C, a substitutional solid solution forms; below this temperature the alloy is composed of a dual phase, α + β. The phase diagram illustrates two conjugate phases, the first between the two solid phases and the second during melting, from solid to liquid. The solidus and liquidus show that the melting point increases with Nb content. It is important to note that the information provided within this phase diagram is only represented above 400 °C (Kolli and Devaraj, 2018).

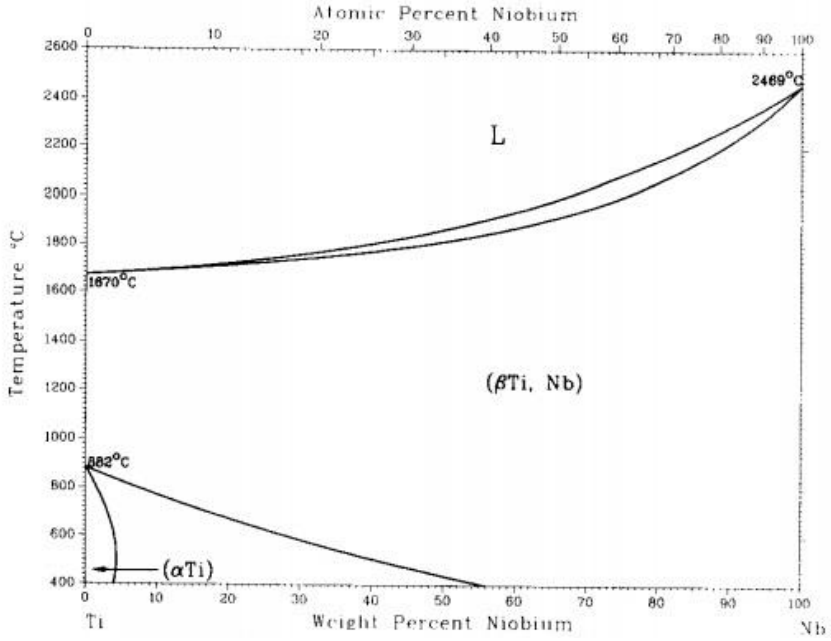

Figure 5: Nb-Ti binary alloy phase diagram (Murray, 1987).

Hon *et al* note that with Nb content greater than 34 wt%, the alloy becomes entirely β-phase with a lower elastic modulus of around 57 GPa (Hon *et al*., 2003). Similarly, Chang *et al* conclude that with increasing content of Nb, the β-phase appears more stable in Ti-Nb alloys, produced using an arc-melting furnace (under

argon atmosphere), before both cold rolling and various solution treatments at various temperatures. The Young's modulus was also shown to be dependent on Nb content, decreasing with increased wt% of Nb; the Ti–30Nb alloys attained values in the range of 45 – 67 GPa. Seemingly, there is a correlation between the alloys Nb content, the structural transformation from α to β phase and the decreasing value of Young's modulus (Chang *et al*., 2016). The observations within the aforementioned studies are in agreement with the phase diagram in Figure 5, although the quantity of Nb content required to produce a stable βTi phase differs significantly. Alternatively, to bulk manufacturing methods, Achache *et al* describe the successful production of Ti-Nb coatings by magnetron sputtering. Deposition occurred, with varying Nb content from 3% to 34%, on glass substrates, with sputtering parameters: argon flow rate; total pressure; and run duration, equal to 50 sccm, 0.43 Pa, and 90 min, respectively. The authors conclude that the alloy's microstructure is closely related to the Nb content and confirm that at 34 wt% Nb the structure is fully composed of β-phase. Suggested by omission, the deposited film, with adequate Nb content, has a β-phase crystal structure without the requirement of any heat treatment (Achache et al., 2015); contrary to powder metallurgy techniques that require high temperatures to form a uniform crystal structure. Achache *et al* have continued their research of Ti alloy systems (deposited by magnetron sputtering), focusing on the quaternary Ti alloy, Ti–23Nb–0.7Ta–2Zr–1.2O at%; chosen due to its "super" properties such as very high strength, low Young's modulus and "superelasticity" at room temperature (Saito *et al*., 2003). The authors conclude that the mechanical properties and phase structure are affected during the sputtering process by the argon flow (working pressure) and negative bias voltage (Achache *et al*., 2016). Other methods of production include; mechanical alloying of powders before spark sintering (Sharma *et al*., 2016), metal injection moulding using elemental powders (Zhao *et al*., 2015) and casting methods (Bönisch *et al*., 2015); although effective these methods are time-consuming and costly. Alternatively, some researchers have resorted to theoretical investigations, such as first-principles Density Functional Theory, DFT, (Liang *et al*., 2016) and d-electron alloy design method (Karre *et al*., 2015), to predict the mechanical properties of various alloy compositions. Although these

methods are effective at predicting numerous properties, the unpredictable nature of biocompatibility, especially when varying elemental composition, would need to be further explored experimentally.

1.3.1.2 *Molybdenum, Mo*

Mo has a bcc structure and contributes to alloy systems by increasing corrosion resistance and hardening (Kuroda et al., 2016). The phase diagram in Figure 6 shows that a substitutional solid solution of βTi, in which Ti and Mo are completely miscible above the transformation temperature of pure Ti, 882 °C. Below this temperature Mo has restricted solubility within an αTi solid solution. The phase diagram also shows a monotectoid reaction, with slow cooling through the monotectoid temperature, at ≈ 21% Mo content a transformation occurs from a single phase microstructure to a lamellar structure. A metastable extension of the stable-equilibrium boundary is also indicated using a dashed line (Baker, 1992). The alloy begins melting between 1670 °C and 2623 °C, dependent on the Mo content. It is important to note that the information provided within this phase diagram is only represented above 400 °C.

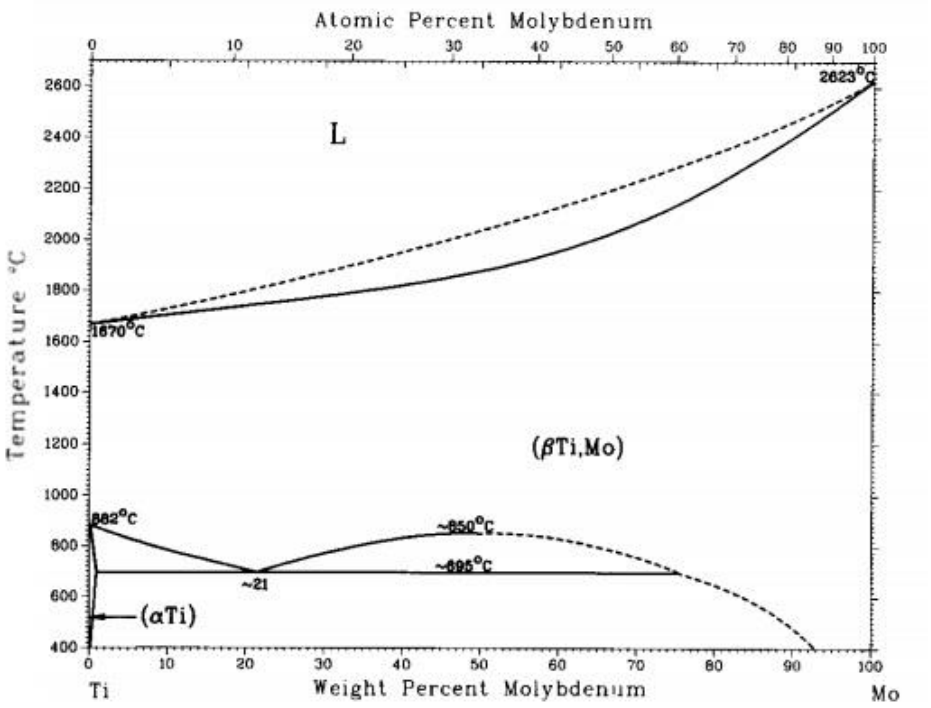

Figure 6: Mo-Ti binary alloy phase diagram (Murray, 1987).

Ho *et al* conducted a comparative study of the mechanical properties of Ti-Mo binary alloys with Mo contents ranging from 6 to 20 wt%. They concluded that when the Mo content was increased to 10 wt% or higher, β-phase became the dominant phase. They also noted that Ti-10Mo had the highest Young's modulus,

while Ti-15Mo had the lowest. The effects of Mo content on the alloys biocompatibility were not investigated (Ho *et al*., 1999). Other comparative investigations include: the crystal phase analysis and preliminary electrochemical studies of Ti–Mo alloys from 4 to 20 Mo wt%, produced using arc-melting (Oliveira and Guastaldi, 2006); the mechanical properties and crystal phase analysis of Ti-Mo alloys with Mo contents ranging from 5 to 20 wt%, again manufactured using arc-melting (Chen *et al*., 2006); and lastly, the observation of differences in the mechanical properties of, commercially pure Ti, Ti–6Al–4V, Ti–13Nb–13Zr and Ti–7.5Mo, produced using casting methods (Lin *et al*., 2005). Researchers concluded, similarly to Nb, that with greater wt% of Mo, binary Ti-Mo alloys have an almost exclusive β phase structure. Oliveira *et al* retierate that Ti-Mo alloys with Mo content at 10 wt% or greater, significantly retain β-phase structure. Electrochemical studies performed, indicated a valve-metal behaviour, where the metal forms an oxide film of uniform thickness and stoichiometry (Bockris, 2013), and good corrosion resistance in aerated Ringer's solution for all alloys (Oliveira *et al*., 2007). Chen and co-authors, propose Ti-10Mo as the most suitable alloy system with consideration of the mechanical properties, obtaining values for compression strength, compression ratio and elastic modulus, equal to 1636 MPa, 22.5% and 29.8 GPa, respectively. In comparison to previous studies, the authors conclude that the improvement in plasticity of Ti-Mo alloys is related to the increase in Mo content (Chen *et al*., 2006). The studies mentioned included only phase structure analysis and mechanical properties testing, with none of the alloys tested biologically for cytotoxicity or adverse tissue reactions.

ATI 15Mo™ Alloys (UNS R58150) is a beta titanium alloy capable of a wide variety of properties including low modulus of elasticity, high strength, excellent fatigue strength, good ductility/formability, exceptional corrosion resistance, and well-documented biocompatibility (*ATI*, 2014).

1.3.1.3 *Tantalum, Ta*

It is well known that Ta possesses a body-centred cubic, bcc, crystal structure; its high corrosion resistance and excellent biocompatibility, like Ti, have also been of interest to many researchers. The phase diagram, shown in Figure 7, illustrates a substitutional solid solution of βTi, in which Ti and Ta are completely miscible above the transformation temperature of pure Ti, 882 °C. The alloy begins melting between a significant temperature range, 1670 °C and 3020 °C, dependent on the Ta content. The solidus and liquidus show that the melting point increases with Ta content. The conjugate phase between the two solid phases is metastable and dependent on the cooling rate, illustrated on Figure 7 by a dashed line (Baker, 1992). It is important to note that the information provided within this phase diagram is only represented above 400 °C.

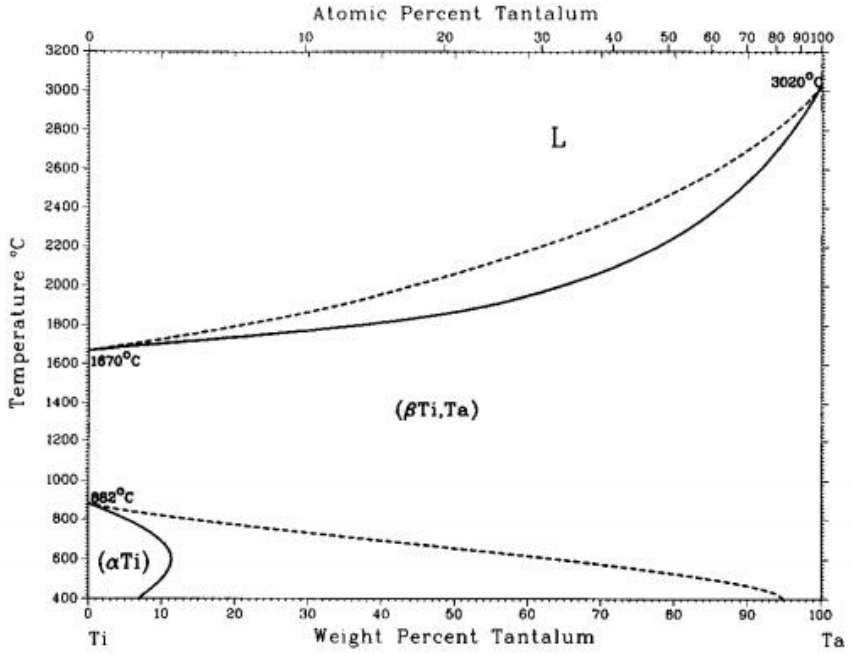

Figure 7: Ta-Ti binary alloy phase diagram (Murray, 1987).

Zhou *et al* investigated the sensitivity of Ta content on binary Ti-Ta alloys. Ti-Ta alloys with Ta contents varied from 10 to 80 wt% were prepared using a tri-arc furnace, under argon atmosphere, before rolling at an unspecified temperature and solution treating at 1223 K. The authors conclude that with Ta content below 20% the alloy exhibits a hcp, α-phase structure and at Ta contents above 60% the alloys

structure is composed of a single metastable, β-phase structure. The Ti-70Ta wt% alloy, with metastable β-phase, was shown to have a much lower modulus than the other alloys investigated (Zhou *et al*., 2004). Zhou *et al* continued their studies of binary Ti-Ta alloy systems, investigating the corrosion resistance and biocompatibility of three, binary Ti-Ta alloy systems, Ti-10Ta, Ti-30Ta and Ti-70Ta wt%, in comparison with commercially pure Ti and Ti-6Al-4V. Unfortunately, the preparation methods employed to produce the alloys are only vaguely described. The authors assess corrosion resistance using anodic polarisation tests and performed biocompatibility testing using L-929 cells, derived from mice. The biocompatibility results showed promise in comparison with commercially pure Ti and Ti-6Al-4V; however, by using mouse derived cells, this is only a guide to biocompatibility, where the results are not always comparable to those obtained using human cells, both *in vivo* and *in vitro*. The authors conclude that both the corrosion resistance and biocompatibility of the three alloy systems was similar to or exceeded those of commercially pure Ti or Ti-6Al-4V (Zhou *et al*., 2005). Alongside conventional manufacturing techniques, researchers are also investigating the properties of binary Ti-Ta alloys using theoretical methods, previously mentioned with regards to Nb, such as DFT. Wu *et al* model the elastic properties and the electronic structure of β-type Ti-Ta alloys from first-principle calculations based on DFT. The authors imply that the stability of the β-phase is improved with increasing content of Ta (Wu *et al*., 2010). Ojha and Sehitoglu, also employ DFT to model binary Ti-Ta alloys, establishing and comparing the lattice constants and associated energies of the bcc-hcp transformation in Ti-6.25Ta at% and Ti-6.25Nb at% alloy systems (Ojha and Sehitoglu, 2016)**.** Morgado *et al* compared the Young's moduli and wear behaviour of two binary, Ti-Ta alloys, Ti-30Ta wt% and Ti-52Ta wt%, produced by laser cladding. The authors conclude that both alloys possess a low Young's modulus; however, Ti-52Ta wt% presents wear behaviour more suitable for the application intended (Morgado *et al*., 2016).

1.3.1.4 *Zirconium, Zr*

As previously mentioned, Zr is classified as a neutral element with regards to phase stability. It has a hcp structure, like Ti, meaning Ti-Zr binary alloys possess an α-phase structure, at temperatures below ≈ 605 °C, and consequently a relatively high Young's modulus. The phase transformations are shown in Figure 8. Interestingly, its addition to Ti-alloys can influence the β-phase, decreasing the β-transus temperature, when in the presence of another β-stabiliser (Correa *et al*., 2015; Kuroda *et al*., 2016; Murray, 1987).

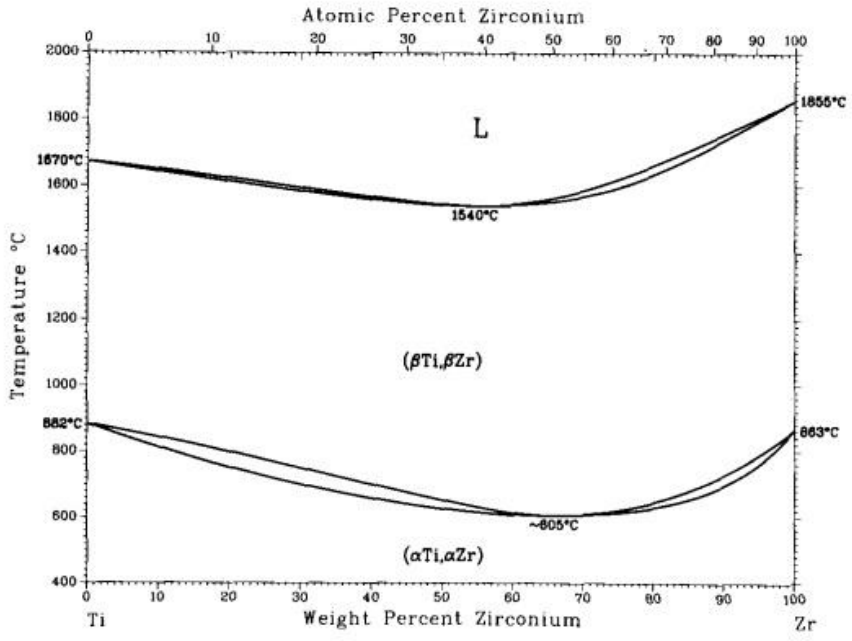

Figure 8: Ti-Zr binary alloy phase diagram (Murray, 1987).

Zr has also been shown to improve the corrosion resistance of Ti-alloys when compared to pure Ti (Han *et al*., 2014); although in contradiction, Oliveira *et al* suggest through the observation of transpassivation at potentials smaller than 8 V, that the addition of Zr in the Ti-50Zr at% alloy encouraged pitting corrosion (Oliveira and Guastaldi, 2006). Where transpassivation is the phenomenon that a metal starts to corrode at an increasing rate relative to the increase in electrode potential (Song, 2005).

1.4Research Aims and Objectives

The research aim of this work was: to develop and demonstrate a systematic approach that enables the primary determination of some of the intrinsic properties that a biomaterial must possess. The research aim will be achieved by developing and evaluating the structural, mechanical and biological properties of β phase binary Ti-alloys (Ti_{100-X} -XNb, Ti_{100-X} -XMo, where X = 15, 25, 50 at%) produced by magnetron sputter deposition.

2. Vacuums and Magnetron Sputtering

Included in this section is: an overview of vacuum systems and a summary of chemical vapour deposition, CVD, and physical vapour deposition, PVD, techniques with particular reference to magnetron sputter deposition.

2.1Vacuum Systems

The general term 'vacuum' covers a range of pressures, subdivided into categories from atmospheric pressure to ultra-high vacuum:

Atmospheric pressure: 1×10^{5} Pa

Low vacuum: $1 \times 10^{5} – 1 \times 10^{3}$ Pa

Medium vacuum: $1 \times 10^{3} – 1 \times 10^{-1}$ Pa

High vacuum: $1 \times 10^{-1} – 1 \times 10^{-7}$ Pa

Ultra-high vacuum: $1 \times 10^{-7} – 1 \times 10^{-10}$ Pa

High vacuums are achieved by first using a roughing pump to evacuate the chamber from atmospheric pressure to ≈ 1×10^{-1} Pa. A secondary pump is then required to increase the vacuum to the desired pressure. The time taken to achieve the required level of vacuum can vary depending on the variables such as the vacuum apparatus used, the volume of the evacuation chamber and the extent of outgassing. Outgassing is the slow deterioration of the vacuum due to the release of adsorbed gasses from the interior surfaces of the vacuum system. Factors such as adsorption, diffusion and permeation contribute to outgassing (Chambers, 2005).

2.2Magnetron Sputter Deposition System

Magnetron sputtering, performed in a controlled argon atmosphere, is a PVD technique widely used in industries such as automotive, construction, electronic and aerospace, to manufacture thin films and produce a variety of different coatings. PVD is a general description given to a variety of surface engineering, vacuum deposition processes, where the material goes from a solid phase to a

vapour phase, then condenses on a substrate in the form of a thin film. Table 1 compares some alternatives to magnetron sputtering, including an overview of the process, advantages and disadvantages.

Table 1: Alternative deposition techniques

Method	Process overview	Advantages	Disadvantages
Magnetron Sputtering	Glow discharge plasma, confined by magnets, bombards a target material, which is "sputtered" and condenses on a substrate.	Low ongoing cost and time efficient. High adhesion strength. Metallic alloys are easily adapted.	Line of sight process.
Chemical Vapour Deposition	Heating of the gas precursors forms a reactive gas mixture. The reactants are absorbed on the substrate surface after mass transport of the reactant gas through a boundary layer to the substrate. A reaction of the absorbents occurs to form the deposited layer.	Low waste deposition.	High temperatures required (restricts use of some substrates). Precursors are often toxic or hazardous.
Ion Plating	The metal coating is evaporated into an inert atmosphere using a low voltage arc at a given temperature. The ionized particles are then accelerated from the plasma by a negative bias onto the substrate.	Inert or reactive atmosphere.	Line of sight process. Often poor quality films.
Plasma Spray	A direct current between a water-cooled copper anode and a tungsten cathode ionises a flow of gas (usually argon) to form a plasma. The powder coating is heated to a molten state by the plasma before being propelled towards the substrate.	Wide range of materials. High quality. Wide range of substrates.	Line of sight process. Automatically operated. High oxide levels in metallic coatings.
Electric Arc Spraying	Electric arc present between the ends of two wires melts the wire, whilst a jet of gas blows the molten droplets towards the substrate.	Easy to vary coating thickness. Low power input.	Low bond strength. Not suitable for ceramics.

The setup of a magnetron sputtering rig consists of a vacuum chamber enclosing a substrate holder positioned in line of sight of a target. The chamber is initially evacuated to a rough vacuum before achieving a high vacuum with the addition of a

secondary pump (a description of the vacuum pumps and gauges typically used can be found in Appendix B). A sputtering gas, commonly argon, is introduced into the chamber. A high potential difference, between two electrodes, is used to accelerate free electrons, which collide and ionise the sputtering gas, initiating plasma. Plasma is a partially ionised gas, containing ions, electrons and neutrals, which is created at reduced pressures via an applied electric field. In PVD processes, the type of plasma used is termed a 'glow discharge', because of the characteristic light given off by the target material and the process gases used. In the basic sputtering process, a target (or cathode) plate is bombarded by energetic ions generated in a glow discharge plasma in front of the target. The bombardment of ions causes the removal of target atoms known as "sputtering"; these atoms may then condense on a substrate as a thin film. Secondary electrons are also emitted from the target surface as a result of the ion bombardment. These electrons help to maintain the plasma.

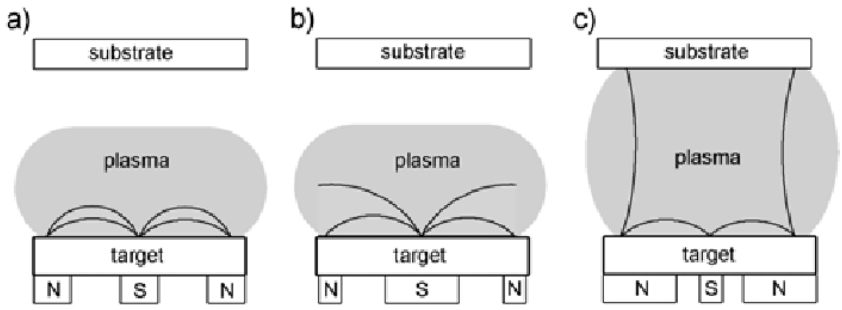

Figure 9: Schematic image of three different planar magnetron configurations with the magnetic field lines indicated. a) balanced magnetron, b) unbalanced type I, and c) unbalanced type II.

Magnetrons make use of the fact that a magnetic field parallel to the target can constrain a secondary electron motion to the vicinity of the target. The magnets are arranged in such a way that one pole is positioned at the central axis of the target with a second pole formed by a ring around the outer edge of the target. This increases the probability that an ionising electron-atom collision may occur. Higher sputtering rates are achieved by the increased ion bombardment of the target. The strength of the magnets is varied in different configurations to further confine the

plasma, Figure 9 illustrates three configurations; type II is the configuration generally used.

Through the introduction of a reactive gas, the magnetron sputtering process enables the production of either thin films of a pure alloy or as a compound film such as a nitride, oxide or carbide. The use of two or more magnetron sources, or blending metallic powders together, enables the deposition of alloy films.

The magnetron discharge can be driven by either direct current, DC, pulsed DC, alternating current, AC, or radio frequency, RF. When using pulsed DC, the applied voltage is periodically switched between negative, pulse-on, and positive, pulse-off. The periodic voltage reversals are designed to reduce arcing during sputtering and provide a stable deposition process. During the pulse on period, positive ions sputter the target material and during the pulse off period, an electron current is drawn at the target that dissipates any charge build-up before an arc event can occur.

The growth of thin films, produced using magnetron sputtering, begins by nucleation, the first atoms arrive randomly at the substrate and establish a permanent residence; these atoms are said to be condensing (Ohring, 1991).

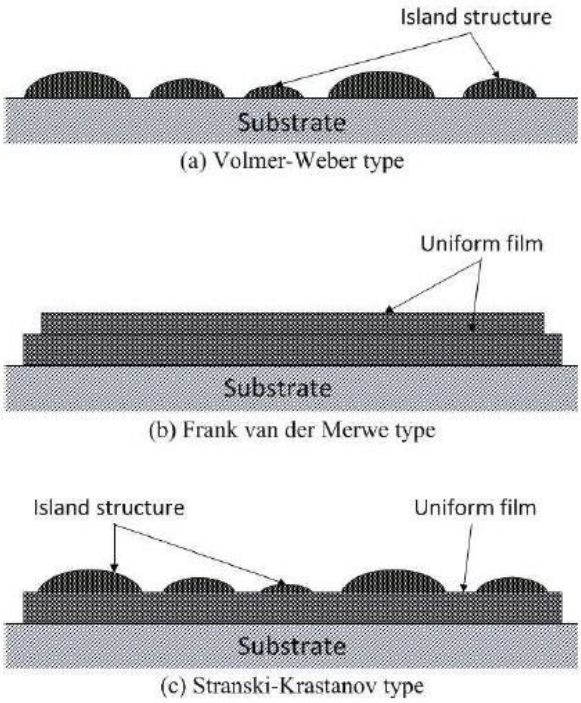

Figure 10: Three modes of thin film growth processes: a) Volmer-Weber type, b) Frank van der Merwe type and c) Stranski-Krastanov type (Ratova, 2013).

The way in which the thin film continues to grow depends on the thin film material and its interaction with the substrate, several models have been suggested to describe the initial growth (Kelly 1997), illustrated in Figure 10: Volmer-Weber type, an island structure, consisting of clusters of atoms nucleating in three dimensions, forming as a result of the atoms being more strongly bound to each other than the substrate; Frank-van der Merwe type, the atoms form uniform mono-layers resulting from the atoms preference to the substrate as opposed to each other; Stranski-Krastanov type, a combination of both preceding types where subsequent mono-layer growth becomes less favourable and islands begin to form (Adachi *et al*, 2012; Brune, 2001). Continued growth is more likely to occur in the elevated regions, leading to a columnar microstructure (Ratova, 2013). However, the type of continued growth, after the formation of several angstroms of the sputtered material, depends heavily on the sputtering and thermodynamic parameters (Adachi *et al*, 2012). Several structural-zone models are used to predict the microstructure of thin films; Thornton proposed a model dependent on two deposition parameters, total argon pressure and substrate temperature, enabling the prediction of one of four possible microstructure outcomes; Zone 1, thermally

unstable, fine-textured, fibrous grains due to low diffusion of surface atoms, Zone 2, densification of the film and growth of the grain sizes, Zone 3, well defined crystals of the sputtered material, and Zone T, dense crystalline structure with small grains (Thornton, 1974).

3. Characterisation Techniques

3.1 Scanning Electron Microscopy

Scanning electron microscopy, SEM, is a non-invasive technique that produces an image of a sample. Within a vacuum, electrons emanating from an electron gun are accelerated, through a high potential difference, and directed using an arrangement of magnetic lenses, towards a sample. The incident electrons cause the emission of k-shell, low-energy electrons (secondary electrons) from the sample atoms prior to the high-energy electrons scattering (backscattered electrons). Multiple detectors recognise the emerging electrons by their energy. The secondary electron detector consists of an anode, with a positive bias applied to collect the emerging electrons. As the beam progressively scans over the sample, the varying anode current, due to the differing number of electrons collected, is converted into an image of the sample's surface (Freedman, 2012). Figure 11 illustrates a typical SEM arrangement.

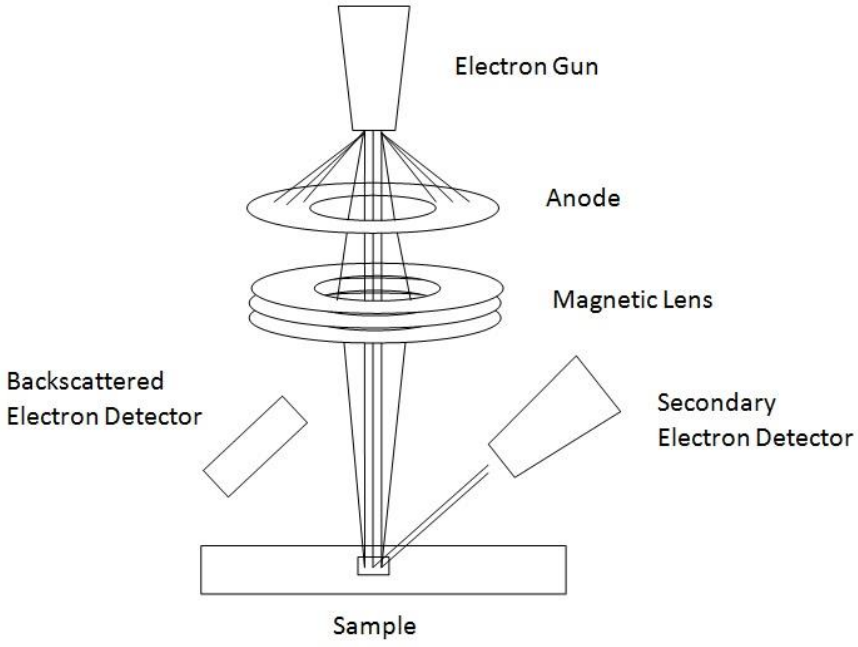

Figure 11: Schematic illustration of SEM.

3.2 Energy Dispersive X-Ray Spectroscopy

Energy-dispersive x-ray spectroscopy, EDX, is an analytical technique used for elemental analysis of a solid sample; generally used in partnership with SEM. When an atom becomes excited, through the bombardment of electrons, it emits an X-ray photon with energy characteristic of the element and the number of characteristic photons is proportional to the element concentration. These photons are detected, enabling the elemental composition of the specimen to be measured through the production of an EDX spectrum. Figure 12 shows the regions from which different signals are detected. The penetration depth, and therefore the emanating signal of characteristic X-ray photons, is dependent on the acceleration voltage and the density of the sample analysed. However, it is generally accepted that the penetration depth into a sample is 1-2 µm. The detection accuracy is also dependent on multiple factors but is generally accepted as 1000 ppm (Whiteside *et al*, 2016).

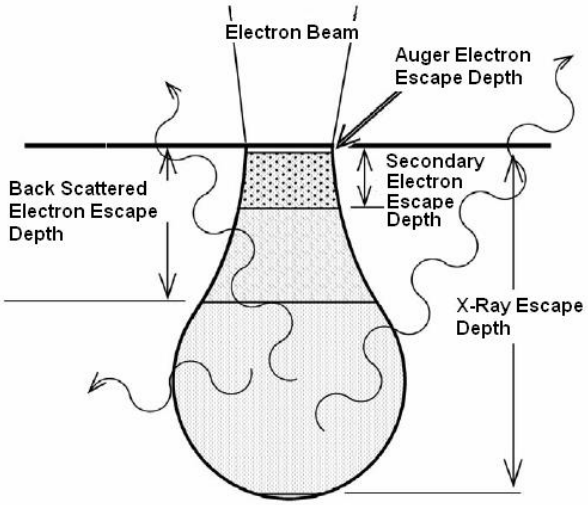

Figure 12: Schematic illustrating the area from which characteristic X-rays emanate. (Hafner, no date)

3.3X-Ray Diffraction

X-ray diffraction, XRD, is a non-destructive analytical technique used to determine a sample's crystallographic structure and properties, such as phase transitions and unit cell dimensions. The diffractometer is made up of an X-ray tube, sample stage and reflected X-ray detector, shown in Figure 13. The X-ray tube consists of a diode

valve where a high potential difference accelerates electrons, present through thermionic emission, from the cathode towards the anode; contained in a vacuum envelope, all encased to provide adequate cooling, radiation protection and collimation. A number of interactions occur between the high-energy electrons and anode target material atoms, some producing heat and others X-rays. The production of X-rays occurs when the incident electrons knock out inner shell electrons from the anode target material atoms. An electron from the outer shell of the atom then fills the hole created and an X-ray photon is emitted. The X-ray spectra produced, predominantly comprising Kα and Kβ, is characteristic of the anode target material; filtration is needed to obtain a monochromatic beam. Unfortunately, the heat-producing interactions are far more likely to occur than X-ray producing interactions, and less than 1% of the energy deposited on the target of an X-ray tube is converted into X-ray radiation (Hay, 1982).

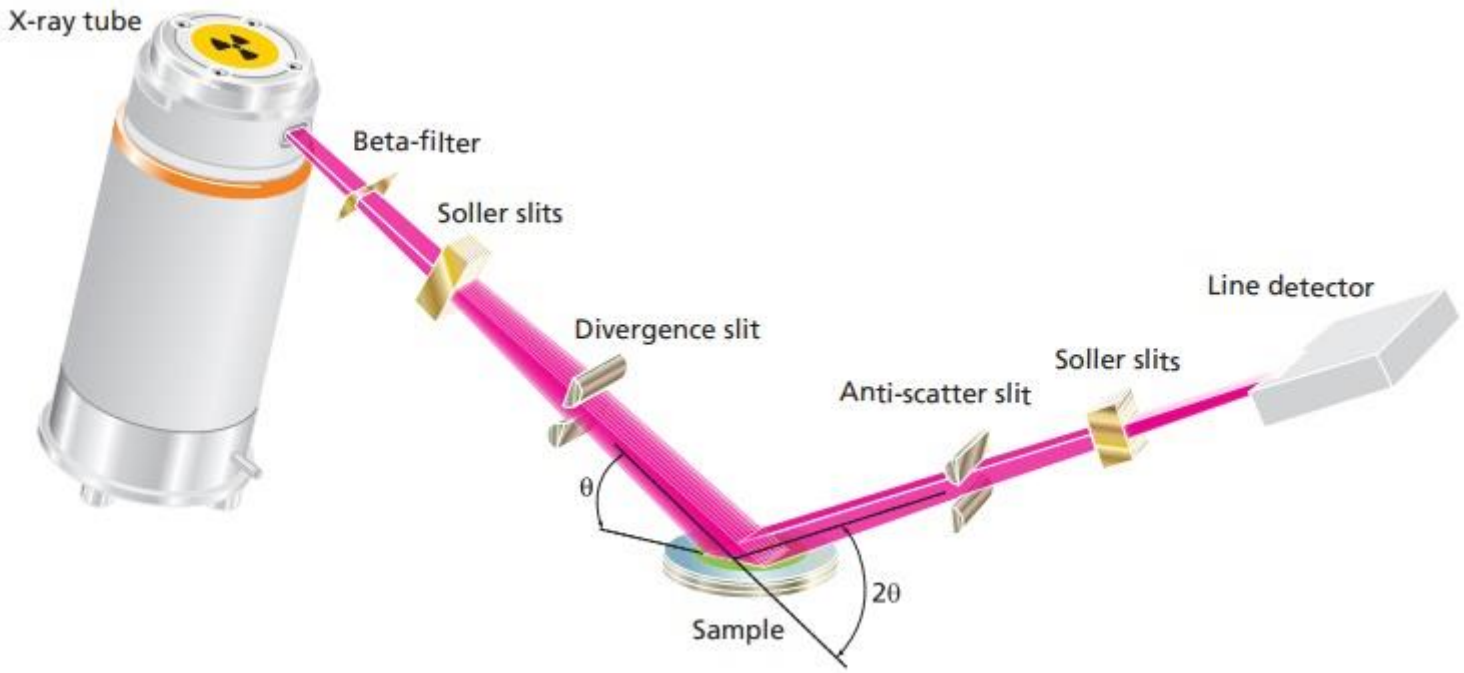

Figure 13: Schematic of XRD apparatus (PANalytical, 2014).

X-rays emanating from the X-ray tube, reflect off the sample before being detected, processed and displayed as a diffraction pattern of count rate against angle 2θ.

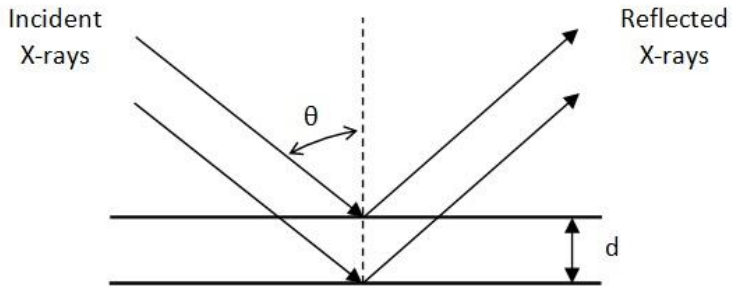

Figure 14: Schematic illustration of Bragg's reflection.

X-rays have a wavelength comparable to the lattice spacing; consequently, when the geometry of the incident X-rays striking the crystal structure of the sample satisfies the Bragg equation, see Figure 14, constructive interference occurs. Bragg's Law relates an integer number, n, of wavelengths of incident electromagnetic radiation, λ, the diffraction angle, θ, and the lattice spacing of the crystalline sample, d.

$$n\lambda = 2dsin\theta \tag{2}$$

Equation 2 gives the relation between the angle and the lattice spacing for a fixed wavelength of X-rays; the lattice spacing is characteristic of the material, enabling the identification of the sample material.

In an amorphous sample the atoms are arranged randomly so no peaks are observed. In a crystalline sample the atoms are arranged uniformly in a repetitive manner; therefore, the above conditions are satisfied. The crystal lattice represents a repetition of the unit cell, where the unit cell is the smallest group of repeating atoms required to maintain the three-dimensional pattern of the entire crystal, illustrated in Figure 15.

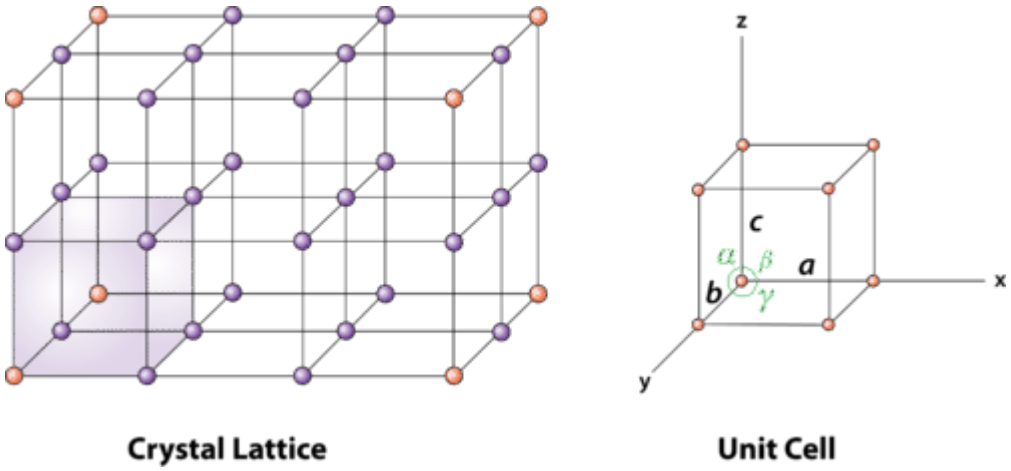

Figure 15: Illustration of the relationship of a unit cell to the entire crystal lattice. Credit: CK-12 Foundation - Christopher Auyeung; License: CC BY-NC 3.0.

In crystallography, Miller indices form a notation system for the crystal lattice planes. A given set of planes with indices, h, k, l, cut the x-axis of the unit cell in h sections, the y-axis in k sections and the z-axis in l sections. The syntax (hkl) represents the interception of the plane; a zero indicates that the planes are parallel to the corresponding axis. In a truly random sample, where the orientation of each grain in a crystalline sample is unrelated to that of its neighbour, the incident X-rays can diffract from each plane equally. However, in reality preferred orientation occurs, where the forming process of the crystalline material influences the arrangement of the crystal structure (Kelly, 1997). Thin films produced using magnetron sputtering are more susceptible to preferred orientation.

3.3.1 Pawley Refinement

Performing a refinement on diffraction data consists of refining an approximate model of the crystal structure, so that the diffraction data calculated using the model structure, resembles the measured data. A Pawley refinement, devised by Pawley in 1981 is one method of refining diffraction data (*Structure Determination from Powder Diffraction Data*, 2006); it enables the determination of reliable cell parameters whilst classifying intensity as a free parameter. A Pawley refinement provides values for comparison including Rprofile, R_p, Rweigthed profile, R_{wp}, Rexpected, R_{exp} and Chi square, χ^2. R_p is the residual difference between observed and calculated plots and R_{wp} uses a weighting function to place more emphasis on

good fit between high intensity data points, such as intense peaks, and less emphasis on low intensity data points, such as background. χ^2, sometimes described as goodness of fit, GOF, is the weighted sum of the squares, of the difference between calculated and observed diffraction patterns.

$$\chi^2 = \frac{{R_{wp}}^2}{{R_{exp}}^2} \tag{3}$$

4. Fabrication and Analysis of Binary Ti-alloys

The project proposes a fast and economic method for preparing and testing various metallic alloys, as a primary step to gather preliminary information about the alloys suitability for the intended application.

Included in this section is: a description of the alloy systems chosen and the reasons thereof, details of the parameters used during magnetron sputtering, results from the experimental techniques used to analyse the alloys, such as SEM, EDX, XRD and alamarBlue® assay, and finally a comparative discussion of the results.

4.1 Alloy Preparation using Magnetron Sputtering

The literature reviewed indicated Mo, Nb and Ta, alongside Ti, as suitable hip prosthesis material alloying elements; Zr was eliminated due to its lack of impact on the β-phase of binary Ti-alloys, as discussed in section 1.3.1.4. In order to validate the methods of fabrication and analysis, Mo, more specifically Ti-15Mo, was selected to enable comparison with the standard ATI 15Mo™ (UNS R58150). Nb's more competitive price, in comparison to Ta, and similarly desirable properties, resulted in it being chosen for this project. Due to the limited time scale of this project, three alloy ratios were chosen, 15, 25 and 50, at%, with Ti as the balance, in order to give a broad indication of how the properties may change with alloy composition variation.

Magnetron sputtering, described in section 2.2, was used to produce thin film samples of six binary Ti-alloys, chosen as a result of their favourable properties described in the literature, with a view to testing both their Young's modulus and cytotoxic effect; 50 at% of Nb, Ti-50Nb, 25 at% of Nb, Ti-25Nb, 15 at% of Nb, Ti-15Nb, 50 at% of Mo, Ti-50Mo, 25 at% of Mo, Ti-25Mo and 15 at% of Mo, Ti-15Mo at%, with Ti as the balance for all the alloys. The large area rig, incorporating two, 300mm x 100mm, planar unbalanced type II magnetrons, attached on top of the chamber, facing a rotating substrate holder, was chosen for deposition, shown in Figure 16 (Ratova *et al*., 2017b).

Figure 16: Photograph of the Large Area Rig at Manchester Metropolitan University.

A Ti target was bolted to one magnetron and either Nb or Mo to the other. Glass microscope slides, 10mm round glass cover slips and silicon wafer substrates were attached to the substrate holder using kapton tape, shown in Figure 17. A DC power supply, dual channel Pinnacle Plus, operating at frequency – 100kHz and Duty – 60% was utilised.

Figure 17: Photographs of the various substrates, attached to the substrate holder using kapton tape, before (left) and after (right) deposition.

The sputtering process took place under the following conditions: Argon flow – 20sccm, Base pressure – $7.0x10^{-4}$ Pa, working pressure ≈ 0.3Pa. The deposition time was 1 hour for all the thin film samples. The current applied to the targets was varied as displayed in Table 2, in correlation with the elemental composition desired. The targets power, corresponding to the applied current, ranged between, 450 – 475W for the Ti target, 100 - 400W for the Nb target and 100 – 400W for the Mo target. The atomic percentage of the relevant elements was obtained using EDX, refer to Table 5. The initial results were used to enable a more accurate estimate of the target current required to obtain the desired elemental composition. In subsequent deposition runs, the current supplied to the target was adjusted accordingly, thus increasing the accuracy of the elemental composition for each alloy. The aforementioned method and parameters were repeated to produce thin film samples in preparation for characterisation and testing.

Table 2: Sample IDs, current supplied to the target, as a percentage, and the respective values for atomic percent.

	Nb target		
Sample ID	Ti-15Nb	Ti-25Nb	Ti-50Nb
Percentage of current supplied to the target	24.3	32.1	52.5
Nb atomic percent, at%	13.1	19.0	44.1
	Mo Target		
Sample ID	Ti-15Mo	Ti-25Mo	Ti-50Mo
Percentage of current supplied to the target	17.9	29.8	48.0
Mo atomic percent, at%	12.9	22.0	43.5

4.2 Characterisation of Samples

4.2.1 SEM

4.2.1.1 *Methodology*

A JEOL JSM-5600LV SEM was used to collect micrographs of the thin film surfaces and fractured cross-sections. Images were taken using an acceleration voltage of 2 kV, the working distance was set between 6 - 9 mm.

4.2.1.2 *Results*

Figure 18 displays SEM micrographs of the six binary Ti-alloy systems, deposited on glass substrates. All the coatings studied appeared to have a relatively smooth surface and some surface defects; however, nodular defects were more prominent in the Ti-Mo alloys.

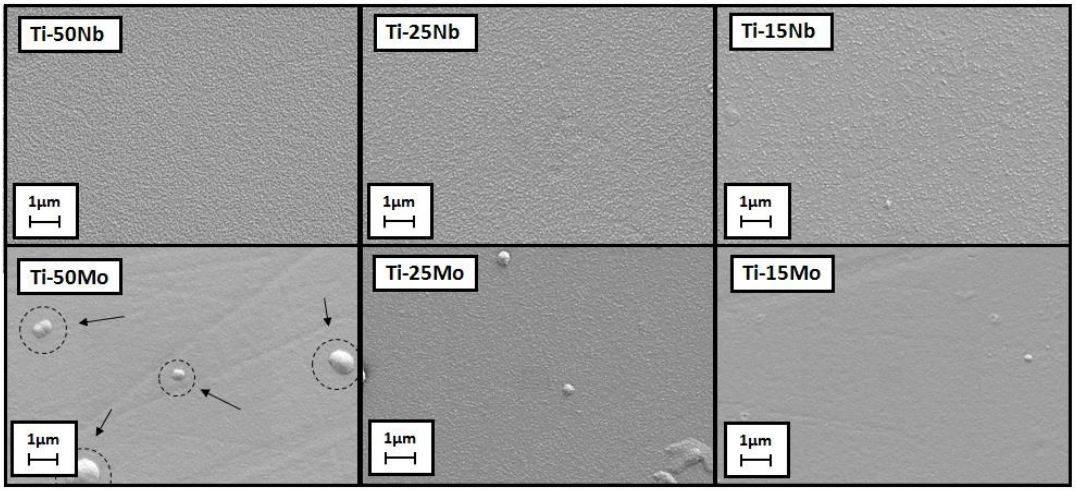

Figure 18: SEM micrographs of Ti-50Nb, Ti-25Nb, Ti-15Nb, Ti-50Mo, Ti-25Mo and Ti-15Mo

The arrows in Figure 18 highlight sample defects, likely resulting from debris left over from the sample preparation; the defects could also be attributed to nodular defects, occurring from either, an irregularity in the substrate surface or a macro-particle created during an arcing event (Brett, 1992).

Table 3: Surface area roughness values for the six binary Ti-alloys.

	Ti-50Nb	Ti-25Nb	Ti-15Nb	Ti-50Mo	Ti-25Mo	Ti-15Mo
Surface roughness, nm	9.91	6.09	5.47	4.93	5.37	6.42

Surface roughness, Ra, analysis was conducted using a Zemetrics brand ZeGauge optical surface profilometer using ZeMaps software. A 10X objective was used with a scan length of 40 µm at a central scan position with a robust scan type. Signal thresholds and saturation thresholds were set to 1.0 % and 10 %, respectively. The mean values obtained for the six alloys were calculated from three measurements across each samples surface and the results are displayed in Table 3.

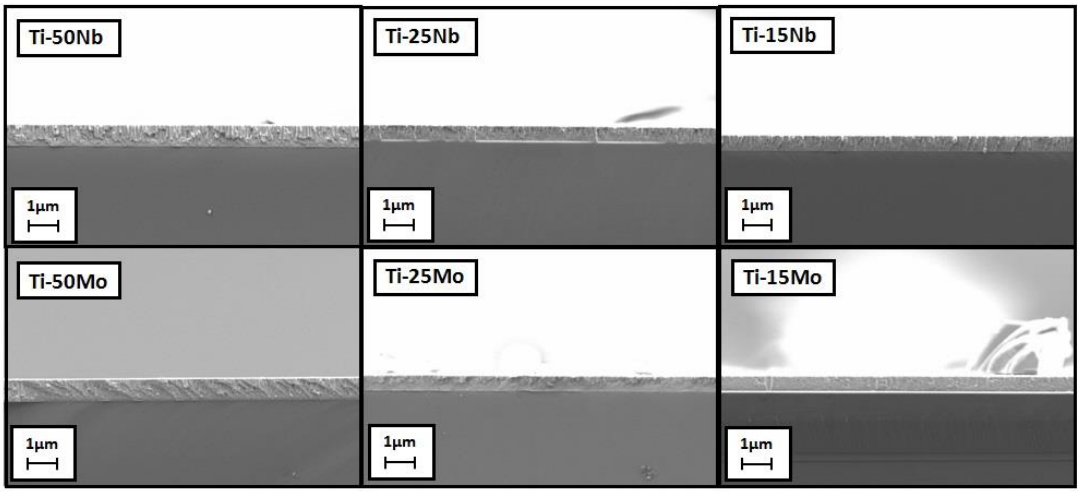

Figure 19: SEM micrographs of fractured Ti-50Nb, Ti-25Nb, Ti-15Nb, Ti-50Mo, Ti-25Mo and Ti-15Mo

Figure 19 shows fractured micrographs of the six binary Ti-alloy systems, deposited on glass substrates taken using SEM. The film growth, across all the coatings is consistent, displaying a dense columnar structure, typical of magnetron sputter coatings (Kim and Choi, 2017). The micrographs also show that none of the coatings appear to have delaminated from the substrate, indicating good levels of adhesion.

The images enabled the determination of the film thickness for each Ti-alloy, presented in Table 4. The variations in film thickness, across the alloys, results from the difference in power used whilst maintaining a constant run time. This variation in film thickness could be eradicated in subsequent deposition runs by adjusting the run time.

Table 4: Film thickness determined using SEM.

	Ti-50Nb	Ti-25Nb	Ti-15Nb	Ti-50Mo	Ti-25Mo	Ti-15Mo
Film Thickness, nm	721	521	563	732	533	527

4.2.2 EDX

4.2.2.1 *Methodology*

EDX analysis was performed on an Oxford Instruments, INCA x-ray microanalysis system with INCA x-sight Si(Li) EDS detector probe and INCA x-stream pulse processor. The x-ray spectrum was collected using an acceleration voltage of 20 kV, working distance of approximately 15mm and magnification of 500x.

4.2.2.2 *Results*

The results for quantitative analysis using EDX are presented in Table 5. The table displays the mean values for atomic percentage, calculated from three values taken at various points across the samples surface, and the ratio of Ti to the alloying element. The accepted values for the ratio were within 2.5% of the desired elemental composition. The EDX results presented in Table 5 indicate the presence of oxygen; however, it is assumed that the oxygen signal emanated from depths below the alloy sample thickness and is therefore from the substrate material.

Table 5: EDX quantitative results

	Ti, at%	Nb, at%	O, at%	ratio Ti/Nb
Ti-50Nb	42.6	44.1	13.3	49.1/50.9
Ti-25Nb	65.5	19.0	15.5	77.5/22.5
Ti-15Nb	75.5	13.1	11.4	85.2/14.8
	Ti, at%	Mo, at%	O, at%	ratio Ti/Mo
Ti-50Mo	41.5	43.5	15.0	48.8/51.2
Ti-25Mo	64.8	22.0	13.3	74.7/25.3
Ti-15Mo	71.9	12.9	15.2	84.9/15.1

4.2.3 XRD

4.2.3.1 *Methodology*

XRD data was obtained using a PANalytical X'Pert Powder diffractometer (Cu-Kα radiation, 40 kV voltage, 30 mA current, 0.06 ° step size and 2.64 s step time).

4.2.3.2 *Results*

The diffraction patterns for the six binary Ti-alloy systems, Ti-50Nb, Ti-25Nb, Ti-15Nb, Ti-50Mo, Ti-25Mo and Ti-15Mo are presented in Figure 20 and Figures 27 to 32, Appendix A. The main βTi peaks are indicated on Figure 20, although, as a result of an additional element into the βTi crystal lattice and therefore difference in atomic radius, an effect on the unit cell parameters is noticeable as the diffraction peaks have shifted from the standard βTi positions.

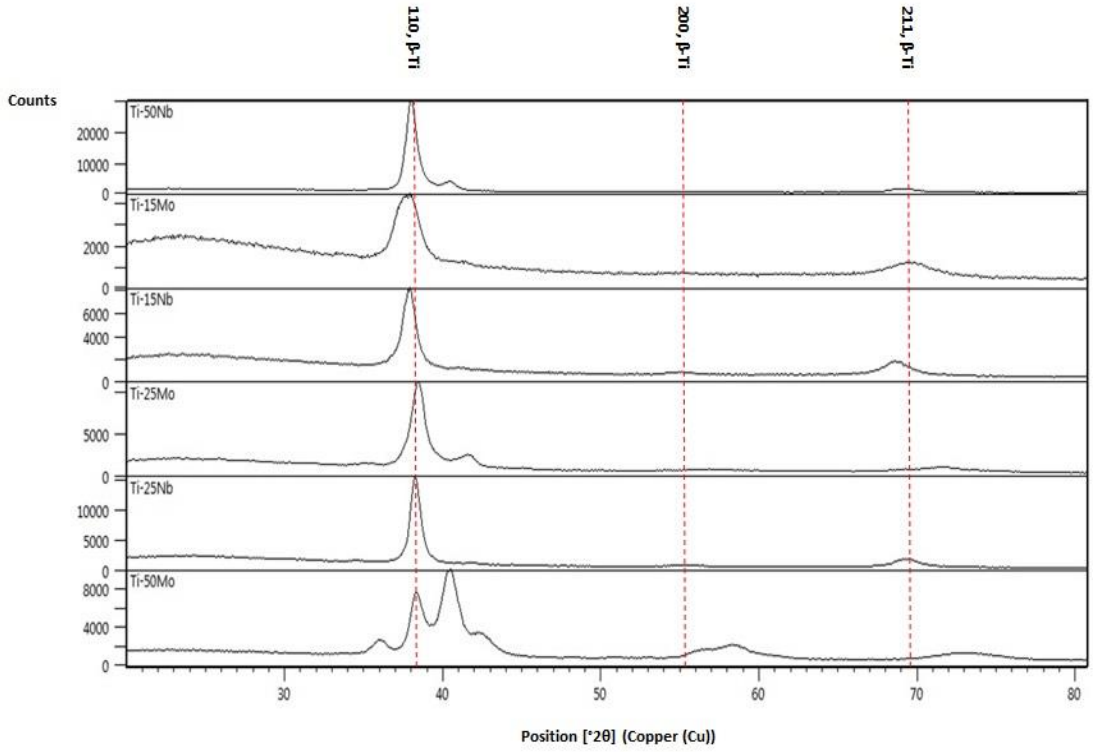

Figure 20: Diffraction patterns of binary Ti-alloys.

4.2.3.3 *Pawley Refinement*

Malvern Panalytical's Highscore Plus (version 4.6a) was used for all XRD analysis. A Pawley refinement was performed on the diffraction patterns for all six alloy

systems. Initially, polynomial background fitting was carried out on the original profile to reduce noise. The region 0-30° 2θ was then excluded from the data, due to an amorphous crest. After refining all necessary parameters, with sufficient cycles, a good fit was achieved; with values for R_p, R_{wp}, and χ^2, presented in Figures 27 to 32, Appendix A. The observed and calculated profiles, represented by the colours black and red, respectively, are shown in Figures 27 to 32, Appendix A.

The Pawley refinement for all six, binary Ti-alloy diffraction patterns, provided evidence of a predominant phase, βTi, with cubic symmetry and space group Im-3m, in all of the six alloys. This correlates with an evident, strong βTi (110) peak at ≈ 38°, visible in all six diffraction patterns, in line with the βTi structural model. In addition to the βTi phase, peaks corresponding to αTi, were present in the diffraction data, detected using the search and match function in the Highscore software package; αTi was therefore included in the refinements, where necessary, as a secondary phase. The unit cell parameters, following refinement, for all six alloys are listed in Table 6.

Table 6: Unit cell parameter results for the Pawley refinement of six binary Ti-alloys. Errors shown in parenthesis.

	βTi Space group: Im-3m, 229	αTi Space group: P63/mmc, 194
Ti-50Nb	a = b = c = 3.334(2) Å	a = b = 2.917(3) Å , c = 4.748(4) Å
Ti-25Nb	a = b = c = 3.08(9) Å	a = b = 3.08(9) Å, c = 4.70(4)
Ti-15Nb	a = b = c = 3.3(4) Å	
Ti-50Mo	a = b = c = 3.38(4) Å	a = b = 3.13(4) Å, c = 5.03(5)
Ti-25Mo	a = b = c = 3.3(6) Å	a = b = 3.1(7) Å, c = 4.6(9) Å
Ti-15Mo	a = b = c = 3.159(3) Å	

The diffraction pattern for both, Ti-50Nb and Ti-25Nb, displayed βTi peaks (110), (200), (211), (220), (310) and (222) peaks indicating a predominantly βTi phase, Figure 27 and 28; however, an unindexed peak, attributed to αTi (101) was also visible within the patterns. The diffraction pattern for both, Ti-15Nb and Ti-15Mo, Figure 29 and 32, mirrored the structural model for βTi, with no unindexed peaks observed.

The binary Ti-alloy, Ti-15Mo, Figure 32, matched the structural model of the βTi phase, with all peaks present. However, with increasing Mo content, the Ti-25Mo alloy and increasingly so with the Ti-50Mo alloy, the αTi phase appeared more prominent, Figure 30 and Figure 31.

4.3 Biocompatibility Studies

4.3.1 NIH 3T3s

An evaluation experiment was designed and undertaken using NIH 3T3 cells to establish the suitability of alamarBlue® when testing metallic thin films; taking particular interest in the elements Ti, Nb and Mo.

4.3.1.1 *Culture of NIH 3T3s*

The 3T3 cells, were cultured using DMEM, supplemented with 1% penicillin-streptomycin, 10% fetal bovine serum and 1% l-glutamine (Lonza, Germany), in T75 Flasks (Thermo Fisher Scientific, USA).

4.3.1.2 *alamarBlue® assay*

The experiment was conducted using two alloy systems, Ti-50Nb and Ti-50Mo, with media only as a control; the 3T3 cells were seeded at a density of 5000 cells per well (48 well plates; Thermo Fisher Scientific, USA). The plates were then incubated at 37°C and 5% CO_2 for 24 hours. After 24 hours culturing, alamarBlue® solution (Thermo Fisher Scientific, USA) was added to each well before incubation for 90 minutes. 100µl medium samples were transferred, in triplicate, into a 96-well plate (Thermo Fisher Scientific, USA), then the fluorescence measured, using a Synergy HT plate reader, with fluorescence excitation wavelength of 530nm and fluorescence emission at 590nm.

4.3.1.3 *Results*

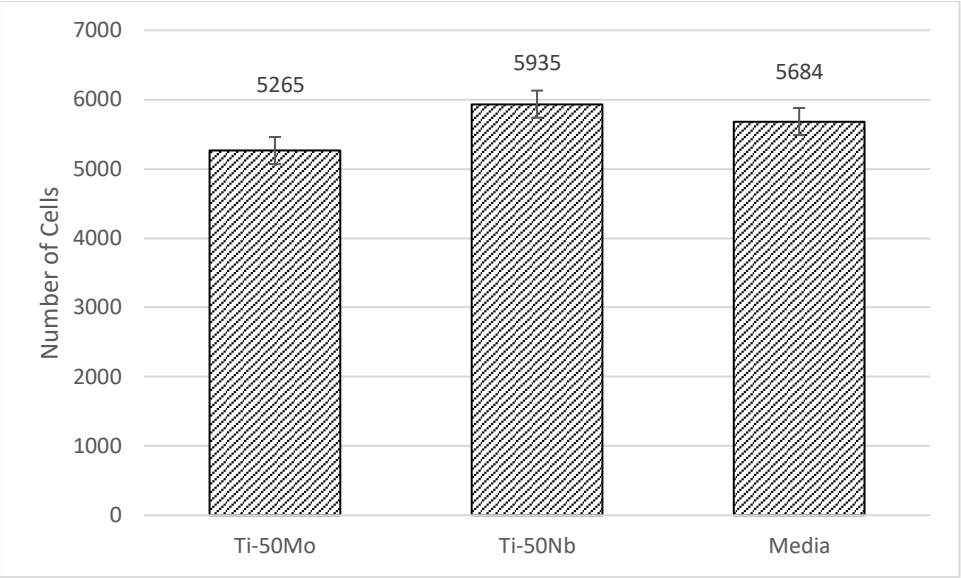

Figure 21: Results obtained using alamarBlue® assay estimating the number of viable 3T3 cells on two binary Ti-alloy systems and a media control; readings were taken after 24hours. Data from one replicate.

The results are presented graphically in Figure 21. The number of cells afters 24 hours appeared similar for both the alloy systems and the media control.

4.3.1.4 *Discussion*

The three significant outcomes from the evaluation experiment were 1. The alamarBlue® was established as a suitable assay, 2. The alloy coatings were very fragile and became detached from the glass cover slips in a significant proportion of cases; this could be attributed to the capillary action of water combined with the low adhesion of the alloy coating to the substrate, 3. Handling and removing the coated cover slips once in the well was very challenging; the experimental results informed future experiments.

4.3.2 hMSCs

The experiment consisted of two parts, the alamarBlue® assay, to access the cell metabolic activity in the presence of the sample, and SEM analysis, to visualise the quality of the cells grown. To prevent loss of the detached coating it was necessary to perform the experiment without changing the media, ensuring the cells were exposed to a pre-ordained sample size. This decision was the preferred option to ensure the validity of the results; although, cell proliferation with time would diminish due to limited nutrients.

4.3.2.1 *Culture of hMSCs*

hMSCs (Lonza, Germany), were resurrected from liquid nitrogen storage, then cultured using mesenchymal stem cell basal medium, MSCBM, supplemented with 10% mesenchymal stem cell growth supplement, 2% l-glutamine and 1% GA-1000 (Lonza, Germany), in T75 flasks (Thermo Fisher Scientific, USA). All the cells in this study were used at passage 4.

4.3.2.2 *alamarBlue® assay*

The alloy samples were placed in wells before the addition of cells at a seeding density of 5000 cells per well (48 well plates; Thermo Fisher Scientific, USA). To ensure the cells remained in contact with the sample, 70µL of cell suspension, containing the desired seeding density, was carefully placed on top of the samples, and then incubated for 30 minutes before the remaining media was added. Samples underwent culture for 7 days; after 1, 3 and 7 days, 10% alamarBlue® solution (Thermo Fisher Scientific, USA) was added to each well before incubation for 90 minutes. 100µl medium samples were transferred, in triplicate, into a 96-well plate (Thermo Fisher Scientific, USA), then the fluorescence measured, using a Synergy HT plate reader, with fluorescence excitation wavelength of 530nm and fluorescence emission at 590nm.

4.3.2.3 *Methodology for Statistical Analysis*

The data collected, calculated using alamarBlue® fluorescence, for the number of cells per time point and Ti-alloy composition, was statically analysed using IBM SPSS

statistics software (version 24); the statistical significance was defined as $p < 0.05$. All experiments were repeated at least three times. The data was first tested for normality using the Kolmogorov-Smirnov test (Ennos, 2012). A two-way ANOVA test was selected to carry out further statistical analysis (Ennos, 2012). Finally, the Post hoc tests, Tukey and Dunnett's, were used to compare the significance, in the number of cells, between groups, between time points, and to compare all the groups against the control, respectively (Ennos, 2012).

4.3.2.4 *SEM Sample Preparation*

SEM investigation was performed to further assess the hMSCs proliferation and morphology. The samples for SEM analysis were placed in wells (6 well plates; Thermo Fisher Scientific, USA), with a seeding density of 5000 cells per well. The difficulty in handling the samples was overcome through the use of larger wells, enabling better access and the removal of samples without causing damage. Alike the method adopted for the alamarBlue® samples, 70 µL of cell suspension was added and the samples incubated for 30 minutes before the remaining media was added. The hMSCs were cultured on top of the six binary alloys for 1 , 3 and 7 days. Following culture, the cells were fixed with 3% glutaraldehyde solution in phosphate buffered saline, PBS (Thermo Fisher Scientific, USA), for 24 hours. The cells were then washed with PBS and an ethanol gradient (20%, 40%, 60%, 80% and 2 × 100% ethanol) to dehydrate the cells. The samples were placed in a desiccator overnight. Finally, the samples were coated with Au, using a Polaron sputter coating system prior to SEM analysis. A JEOL JSM-5600LV SEM was used to collect micrographs of hMSCs cultured on the six binary Ti-alloys.

4.3.2.5 *Results*

The kolmogorov-Smirnov test produced the result $p > 0.05$, therefore the distribution was not significantly different from the normal distribution, enabling data analysis using parametric tests.

The two-way ANOVA showed that the number of cells increased significantly with both the time point ($F = 69.9$) and the type of alloy ($F = 3.016$), however there was not a significant interaction between the time point and the type of alloy. The

Tukey test showed, through the comparison of all the binary Ti-alloys, only two alloys, Ti-50Nb and Ti-50Mo, presented a significant difference, with $p < 0.05$, all other alloy combinations were not significantly different from one another. The Dunnett's test showed that one alloy, Ti-50Mo, was significantly different from the media control, with $p < 0.05$; Figure 22 presents the significance graphically. A clear trend was also evident, although, not statistically assured, that higher Nb content = higher number of cells.

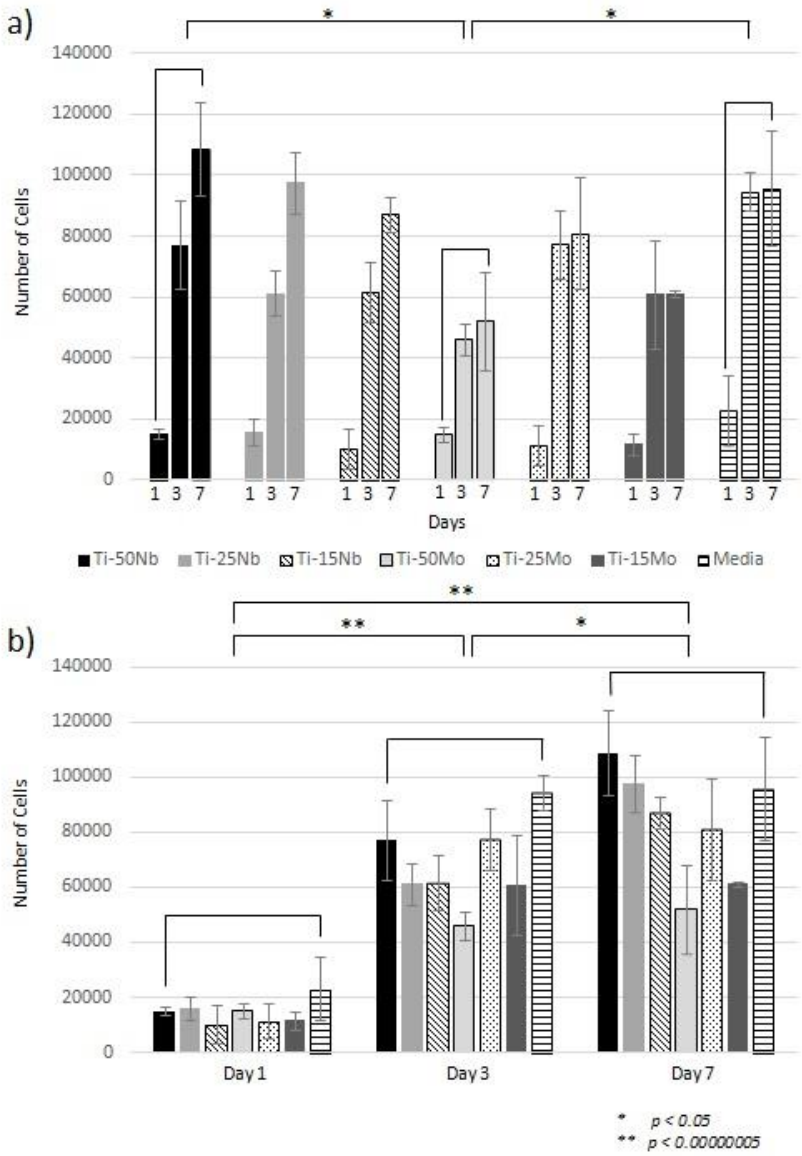

Figure 22: Results obtained using alamarBlue® assay estimating the number of viable hMSCs on six binary Ti-alloy systems and a media control; readings were taken at three time points. a) Results displayed to enable the comparison of the six binary Ti-alloy systems, b) Results displayed to enable the comparison of the three time points. Data from three replicates.

The Tukey test was again used for the comparison of time points, presenting a significant difference between days 1 and 3, days 3 and 7 and days 1 and 7, with values for $p < 0.00000005$, < 0.05 and < 0.00000005, respectively, shown graphically in Figure 22. The statistical analysis undertaken, showed a drop in cell growth between days 3 and 7, compared to days 1 and 3. This supports the prediction that the lack of nutrients, remaining in the media, would cause cell proliferation to diminish; that said the graph provides evidence that the cells multiplied normally between seeding and day 1, and day 1 to day 3.

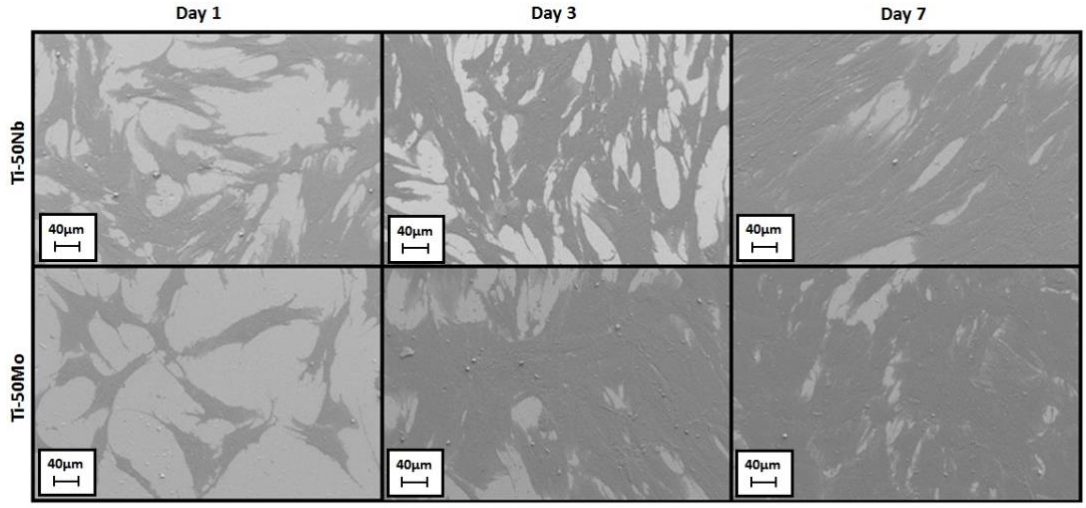

Figure 23: SEM micrographs of hMSCs on Ti-50Nb and Ti-50Mo after 1, 3 and 7 days of growth.

Figure 23 shows the SEM micrographs of Ti-50Nb and Ti-50Mo at day 1, 3 and 7, Figure 24 shows the SEM micrographs of Ti-25Nb and Ti-25Mo at day 1 and 7 and Figure 25 shows the SEM micrographs of Ti-15Nb and Ti-15Mo at day 1, 3 and 7. The hMSCs, cultured onto all the alloys, show a normal spindle cell morphology, with multiple, long pseudopodia, indicating cell interaction and communication. The images also show a tendency for the cells to orientate in a parallel manner.

The micrograph images, in acceptance with the alamarBlue® results, show a clear difference between the three time points. It is therefore evident that the binary Ti-alloys compared, have little or no cytotoxic effect. However, it is not visibly apparent which alloy encourages proliferation most.

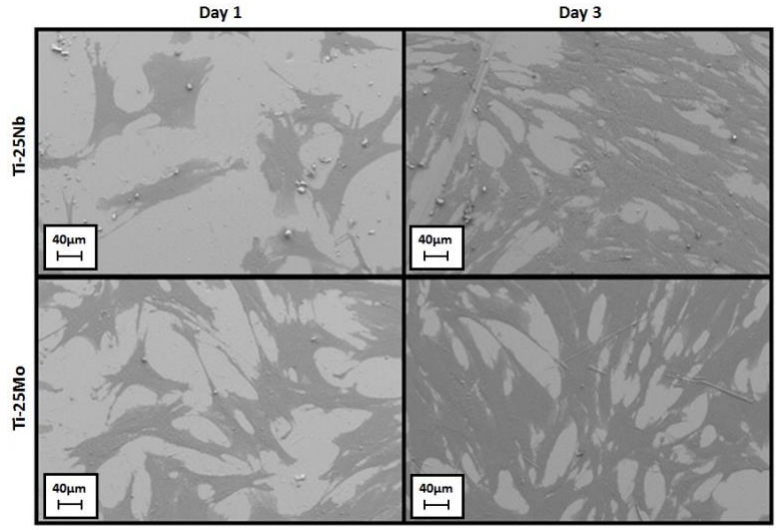

Figure 24: SEM micrographs of hMSCs on Ti-25Nb and Ti-25Mo after 1 and 3 days of growth.

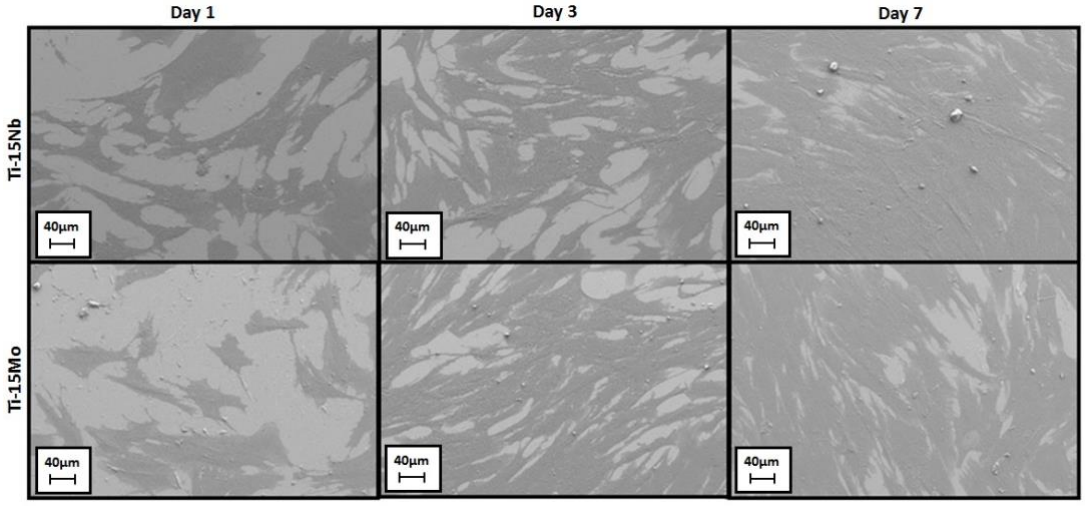

Figure 25: SEM micrographs of hMSCs on Ti-15Nb and Ti-15Mo after 1, 3 and 7 days of growth.

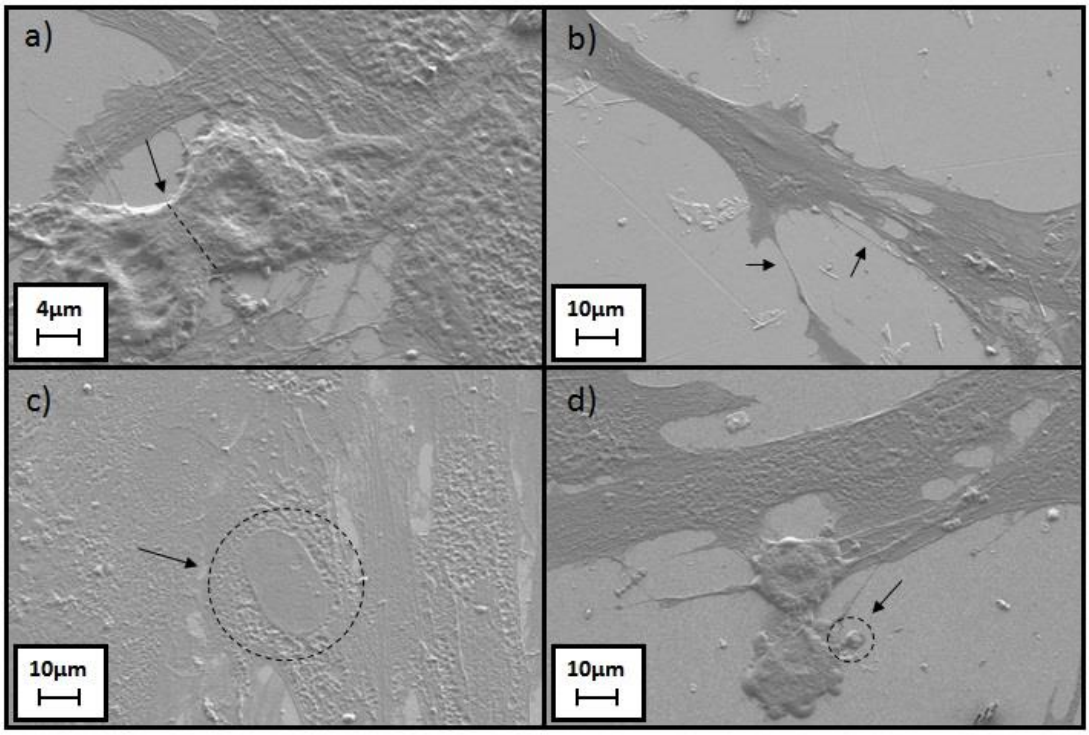

Figure 26: High-magnification SEM micrographs of hMSCs on various Ti-alloys. a) hMSC mitosis on Ti-25Nb, b) morphology of a single cell on Ti-15Mo, c) nucleus of a hMSC on Ti-15Nb and d) early stages of apoptosis of a hMSC on Ti-15Nb.

Figure 26 displays SEM micrographs of individual hMSCs. Figure 26 a) shows the formation of the cleavage furrow, represented by the dashed line, this provides evidence that the cell was undergoing mitosis. Mitosis consist of four stages, prophase, metaphase, anaphase and telophase; the cell presented in Figure 26 a) shows the telophase stage of the process, shortly before the two daughter cells divide completely. Figure 26 b) shows a single hMSC with multiple pseudopodia, highlighted by arrows. The arrow and highlighted area in Figure 26 c) shows the cell's clearly defined nucleus. In Figure 26 d) the cell morphology is beginning to resemble that of an early apoptotic cell, the circled region indicates an apoptotic body (Elmore, 2007). To determine if this is the case, further *in vitro* studies would need to be performed; this would give an indication of the number of cells undergoing morphological changes towards cell death versus the number of viable cells. It is also important to consider the cells dependence on sufficient nutrients and the possible effect of the lack of nutrients in this study, discussed earlier in this section.

4.4 Discussion

Thin film samples deposited using magnetron sputtering, commonly exhibit preferred orientation, indicated by variations in the relative intensity of the diffraction peaks or even the absence of certain peaks from the diffraction pattern (Kelly, 1997; Lee and Lee, 1996). A Pawley refinement reliably refines cell parameters but classifies intensity as a free parameter. The XRD diffraction patterns and subsequent Pawley refinements conducted in this thesis, see Figures 27 - 32, Appendix A, showed that all six alloys have a predominantly β-phase structure; identifiable by the strong peak at ≈ 38° in all the XRD diffraction patterns. The Pawley refinement also suggested the introduction of a two phase structure at the two higher alloying concentrations, 25 at% and 50 at%, in both the binary Ti-alloy systems investigated. Further investigations into the possible presence of transitional phases such as the non-compact hexagonal ω, hexagonal α' and orthorhombic α", would be beneficial but are beyond the remit of this thesis (Bönisch *et al*, 2013; Hickman, 1969; Kolli, 2018; Liu, 2018; Trinkle, 2003). At lower concentrations, the alloy was likely to be a substitutional solid solution, where an atom of one element, was substituted randomly by an atom of a different element, resulting in one crystal phase, in this case βTi. However, at higher concentrations, it appears likely that the structure became saturated and the difference in atomic size resulted in stress occurring within the crystal lattice, this induced stress then caused a re-ordering of the structure and ultimately, the introduction of a secondary phase. Magnetron sputtering is a nonthermal equilibrium technique (Adachi, 2012), where the atoms arriving at the substrate deliver a relatively large amount of energy to the film's surface, through atom bombardment, which is sufficient to form the βTi phase. This energy rapidly dissipates resulting in extremely fast cooling and the freezing of the crystal structure; as a consequence higher atom packing, in substitutional solid solutions, is possible compared with equilibrium techniques (Liu *et al*, 2018; Musil and Bell, 1996). In support of this theory, Bates and Arnell found high levels of solid solubility when investigating the microstructure of three binary Al-alloy systems (Bates and Arnell, 1997). Liu et al prepared Ti-17 alloy films by magnetron sputtering and established that with a

substrate temperature of 125 °C, considerably lower than the β-transus temperature for pure Ti, 882 °C, the structure was entirely metastable β-phase. By altering the substrate temperature a dual phase system was established; the increase in substrate temperature transfers energy to the once immobile atoms enabling them to diffuse through the thin film. Lui et al also describe the phase structure as metastable β-phase, due to the non-thermal preparation technique and the instability of the structure if subjected to thermal or mechanical processing (Liu *et al*, 2018). The thin film alloys prepared in this thesis would also be classified as having metastable β-phase structures (Kolli, 2018).

Researchers have investigated the relationship between microstructure and mechanical properties of thin films deposited by magnetron sputtering, incorporating nano-indentation methods to calculate the Young's modulus. Many studies have shown that β-phase Ti-alloys have a low Young's modulus in comparison to α, near-α and α + β Ti-alloys (Niinomi *et al*., 2012). Unfortunately, for this thesis the nano-indentation equipment required for testing was not available, although, the literature suggests that the binary Ti-alloys investigated would have a relatively low Young's modulus because of their evident β-phase, bcc structure. Marker *et al* used DFT to predict the Young's modulus for five binary Ti-alloy systems, Ti-X (X = Mo, Nb, Ta, Zr, Sn), with bcc lattice structure. The authors calculated values of Young's modulus for Ti-50Nb, Ti-25Nb, Ti-13Nb, Ti-50Mo, Ti-25Mo and Ti-13Mo wt%, equal to 86 ± 10 GPa, 63 ± 13 GPa, 31 GPa, 138 ± 19 GPa, 84 ± 15 GPa and 65 GPa, respectively (Marker *et al*., 2018). Kim *et al* investigated the surface morphologies, surface roughness, electrical, and nano-mechanical properties of binary Ti-alloy thin films, annealed at various temperatures (Kim and Choi, 2017). Achache *et al* investigated the effect of deposition pressure and negative bias voltage on the morphology, microstructure, texture, mechanical properties and super-elastic effect of thin films, Ti-Nb-Zr-Ta, deposited using magnetron sputtering. Cui *et al* studied the mechanical and tribological properties of Ti-doped diamond-like carbon films, deposited on Si substrates at room temperature by magnetron sputtering (Cui et al., 2012). The literature provides evidence that nano-indentation would be a suitable technique for the

determination of the Young's modulus; however it should be considered that thin films may exhibit different and incomparable elastic behaviour from that of bulk materials as a result of the effects of the structure, surface and substrate (Shi *et al*., 1997).

The EDX results suggest the presence of oxygen in the alloys; however, it should be noted that the EDX spectrum produced also suggested the presence of silicon. The signal recorded originates from penetration depths of around 1-2 µm. The thin films produced in this thesis were of thickness < 1 µm, so it is reasonable to assume that a considerable proportion of the X-ray spectrum observed emanated from the substrate material (Whiteside *et al*, 2016).

Exposure of Ti, and its alloys, to air results in the formation of a thin oxide layer (Milosev *et al*., 2000). The oxide layer, of a few nanometres, is responsible for the material's bio-inert and corrosion resistant behaviour (Beutner *et al*., 2010). Research has focused on the formation of an increased oxide layer to act as a barrier layer between the body fluids and the base alloy (Browne and Gregson 1994; Sing Ng *et al*., 2005; Masahashi *et al*., 2012). Satoh *et al* proposed a plasma-oxidation technique, as an alternative to thermal or anodic oxidation methods, for Ti–6Al–4V, in order to suppress the elution of toxic alloying elements into the human body, in the case of this study Al and V; whilst increasing the alloys corrosion resistance. The investigations found that without treatment, the alloy possessed an oxide layer in the single nanometres, and the post treatment oxide layer was approximately 50nm. The authors conclude that the plasma process yields an oxide layer with better barrier properties than that fabricated by the thermal process (Satoh *et al*., 2013). This study and numerous others demonstrate the importance of an oxide layer, which forms a barrier that reduces the likelihood of metallic ions being released, especially when alloying elements that may cause undesirable consequences are used. Further analytical studies, such as argon ion etching prior to X-ray photoelectron spectroscopy, XPS, could be used to determine the thickness of the oxide layer, alongside the distribution of alloying elements in the oxide layer, for the samples produced in this thesis.

Recently, research has focused on the effect the oxide layer has on cell proliferation and differentiation (Santiago-Medina *et al*., 2014; Chiang *et al*., 2009; Yang and Huang, 2010), with some studies investigating whether the oxide layer could be enhanced further to encourage cell proliferation and differentiation. Santiago-Medina et al suggest that TiO_2 is a bioactive factor but speculate whether a reaction between the TiO_2 and the culture medium may result in the release of oxygen and therefore encourage osteoblast differentiation (Santiago-Medina *et al*., 2015). Further investigations are necessary to determine whether this is the case, as TiO_2 could behave differently within the human body.

The results obtained from the alamarBlue® assay using hMSCs showed a higher cell number and therefore proliferation with increasing content of Nb, Figure 22; one possible explanation for this is that the increase in surface roughness with increasing Nb content supported cell growth, see Figure 18 and Table 3. However, in contrast, many studies have shown a decrease in cell number with surface roughness. Martin *et al* prepared samples for culture with MG63 cells, using grade 2, un-alloyed Ti (ASTM F67), with differing surface roughness values, the study concluded that, although difficult to access, the surface roughness and topography inhibited cell replication, displaying decreased cell number, and possibly cell adhesion (Martin *et al*., 1995). Lincks *et al* studied the effect of surface roughness of cpTi and Ti-6Al-4V on MG63 cells; a significant difference was not observed when comparing the smooth surface and rough surface between each sample (Lincks *et al*., 1998). Another study, performed on the effects of surface texture of Ti-6Al-4V on the interaction with human osteo-sarcoma, cells, showed enhanced orientation and attachment with higher surface roughness (Chen *et al*., 2007). Rosa and Beloti, assessed the proliferation of human bone marrow cells, cultured onto commercially pure Ti samples with different surface roughness values. They found that the cell population doublings, and therefore proliferation, decreased with an increase in surface roughness. Rosa and Beloti hypothesise that the degree of osteoblastic differentiation may alter the cells preference with regard to surface roughness (Rosa and Beloti, 2003). The surface roughness values obtained in this thesis are of the nano-scale, in contrast, the results obtained in the literature are all of the

micro-scale; therefore, it is reasonable to assume that such minor variations in surface roughness would not affect cell growth. More recently, Medda *et al* studied the response of hMSCs to gold nano-patterned, Ti-40Nb alloys. The findings show that the overall cell number, as well as cell confluence, on the nano-patterned surface is lower compared to the non-patterned surface (Medda *et al*., 2014). However, the surfaces produced, with nanoparticles of approximately 5nm and average inter-particle distance of 68±13 nm, is not directly comparable with the approximately uniform surfaces produced in this thesis. In addition, the various techniques used to change the surface topography may also have an impact on the surface composition; therefore, it cannot be clarified whether changes in surface chemistry or roughness, or a combined effect of both, underlie the cell responses.

Eisenbarth *et al* studied the biocompatibility of β-stabilising elements. The authors conclude that the viability of both cell types tested, murine calvaria osteoblast-like cells and bovine aortic endothelial cells, were strongly affected by Mo, and ultimately Mo should not be used, at least in large quantities, as a β-stabiliser. The authors did not elaborate on the amount of Mo that constitutes a large quantity (Eisenbarth *et al*., 2004). In agreement, the statistical analysis performed on the results obtained from the alamarBlue® assay using hMSCs showed a significant difference, $p < 0.05$, between both the Ti-50Mo alloy and the Ti-50Nb alloy, and the Ti-50Mo alloy and the media control, Figure 22. The SEM micrographs, Figure 23, provide very little visual evidence of a reduced cell number, and the cells appear to be at a similar confluence to that of all the other alloys; that being said a difference in growth pattern is noticeable; the cells appear less elongated with no noticeable growth orientation. This sporadic growth pattern could be due to the environmental impact created by the discussed toxicity of Mo at high concentrations. The cell morphology and growth, shown in Figures 23 - 25, appeared consistent across all the other Ti-Mo and Ti-Nb alloys, suggesting very little or no toxicity in binary Ti-Mo alloys with Mo content less than 25 at% and no toxicity in binary Ti-Nb alloys.

5. Conclusion

The method proposed enabled the fabrication and characterisation of six binary Ti-alloys. Following fabrication, it was possible to determine the alloys crystal phase structure and elemental composition using XRD and EDX, respectively. Biocompatibility studies using alamarBlue® with hMSCs were performed to assess the alloys' cytotoxicity. Further testing of the alloys Young's modulus using nano-indentation would have been advantageous in deciding the most suitable alloy system from the six chosen; unfortunately, the nano-indentation equipment was not available. Fundamentally, to perform as a suitable hip replacement material, an alloy should possess both a low Young's modulus and no cytotoxicity. The research completed in this project shows that this method of fabrication and analysis is a time and cost efficient method that enables the initial determination of these essential properties.

5.1 Future Work

The method employed to fabricate and characterise the binary Ti-alloys is not restricted to only binary Ti-alloys and could be applied to many different alloy systems, including ternary and quaternary Ti-alloys; this would enable systematic testing of a wide range of alloys, intended as implant materials, based on the fundamental properties needed to succeed, a low Young's Modulus and excellent biocompatibility, before the initiation of further testing. Successively, reactive magnetron sputtering could be used to produce oxide layers of various thicknesses without jeopardising the alloys composition or properties. Other characterisation techniques, such as XPS, post argon etching to determine the thickness of the oxide layer and the concentration of the other alloying elements at the surface, wettability studies (Ratova et al., 2017a), for an insight into the effect the surface's hydrophilic nature has on cellular response, and nano-indentation testing, to experimentally determine the Young's modulus of the alloys, providing a greater understanding of the materials properties and the relationship it would have with the body's environment.

In agreement with the literature, at 15 at%, both the alloys containing Nb and Mo, have a fully β-phase structure; however, at higher concentrations of both Nb and Mo, there is a distinct lack of investigations, in the literature, into the phase structure of binary Ti-Nb and Ti-Mo alloys. More research and experimental investigations, using high-resolution XRD, would help to further understand the microstructure of these alloys.

Further biocompatibility studies would be advantageous to investigate the bio-active nature of the alloys produced, hMSCs cultured in osteogenic media for a minimum of 28days, tested using Alizarin Red S Staining, would enable the determination of the amount of cell differentiation and ultimately an understanding of the osseo-integration properties of the implant material prior to any surface treatment.

Appendix A

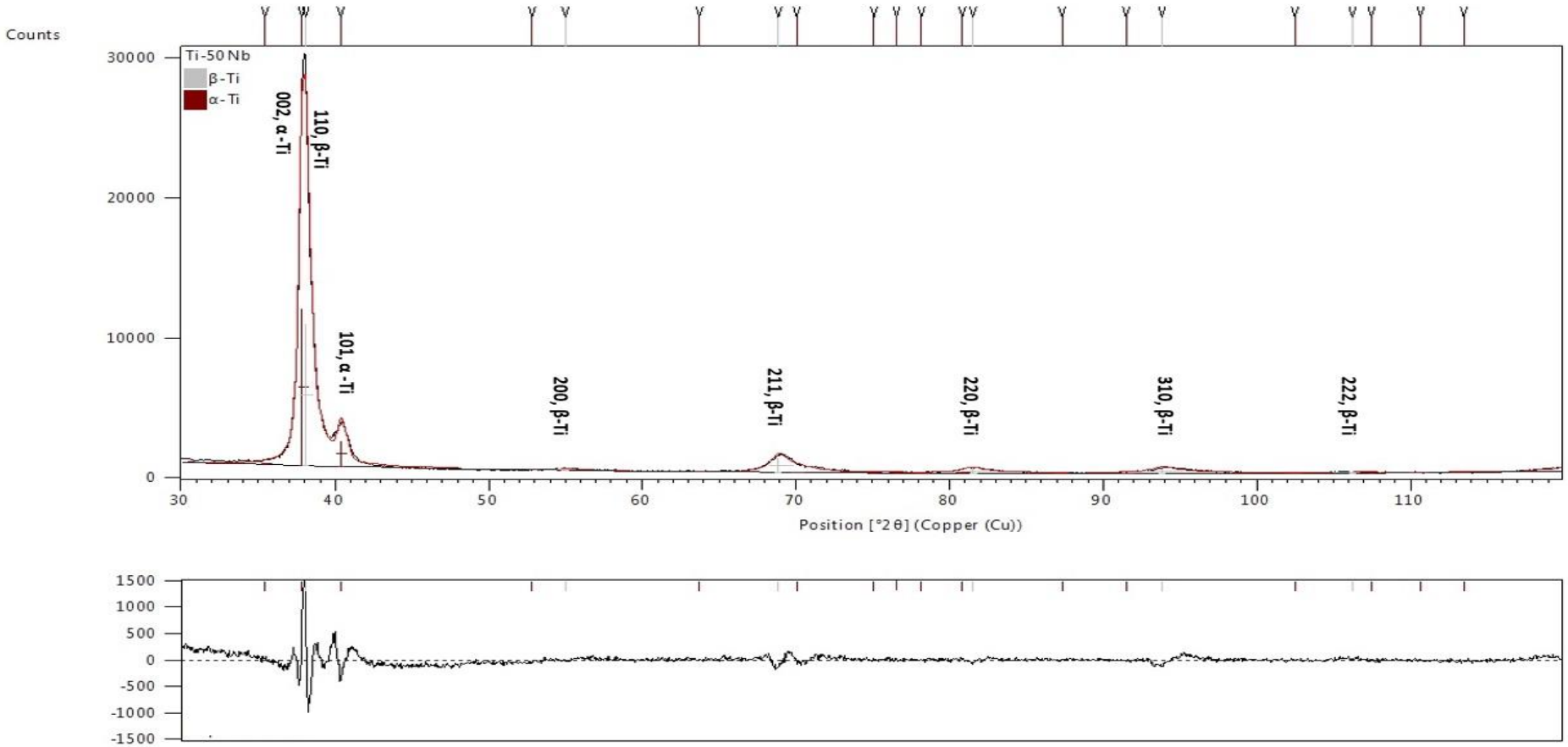

Figure 27: Observed and calculated profiles for the Pawley refinement of Ti-50Nb.The final agreement factors were Rp = 5.712%, Rwp = 7.565% and χ2 = 2.233. The second graph is the difference plot.

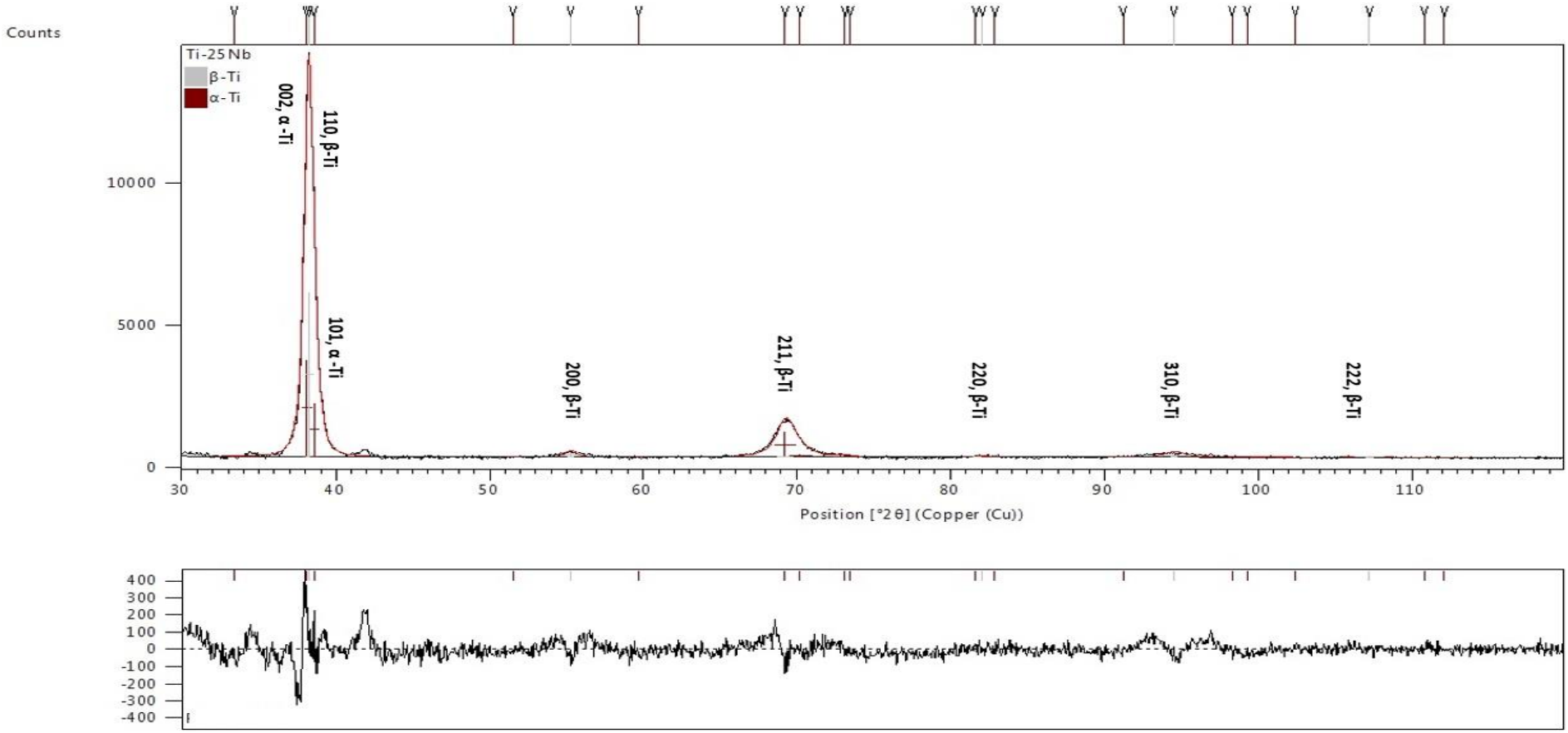

Figure 28: Observed and calculated profiles for the Pawley refinement of Ti-25Nb.The final agreement factors were R_p = 7.463%, R_{wp} = 7.757% and χ^2 = 1.099. The second graph is the difference plot.

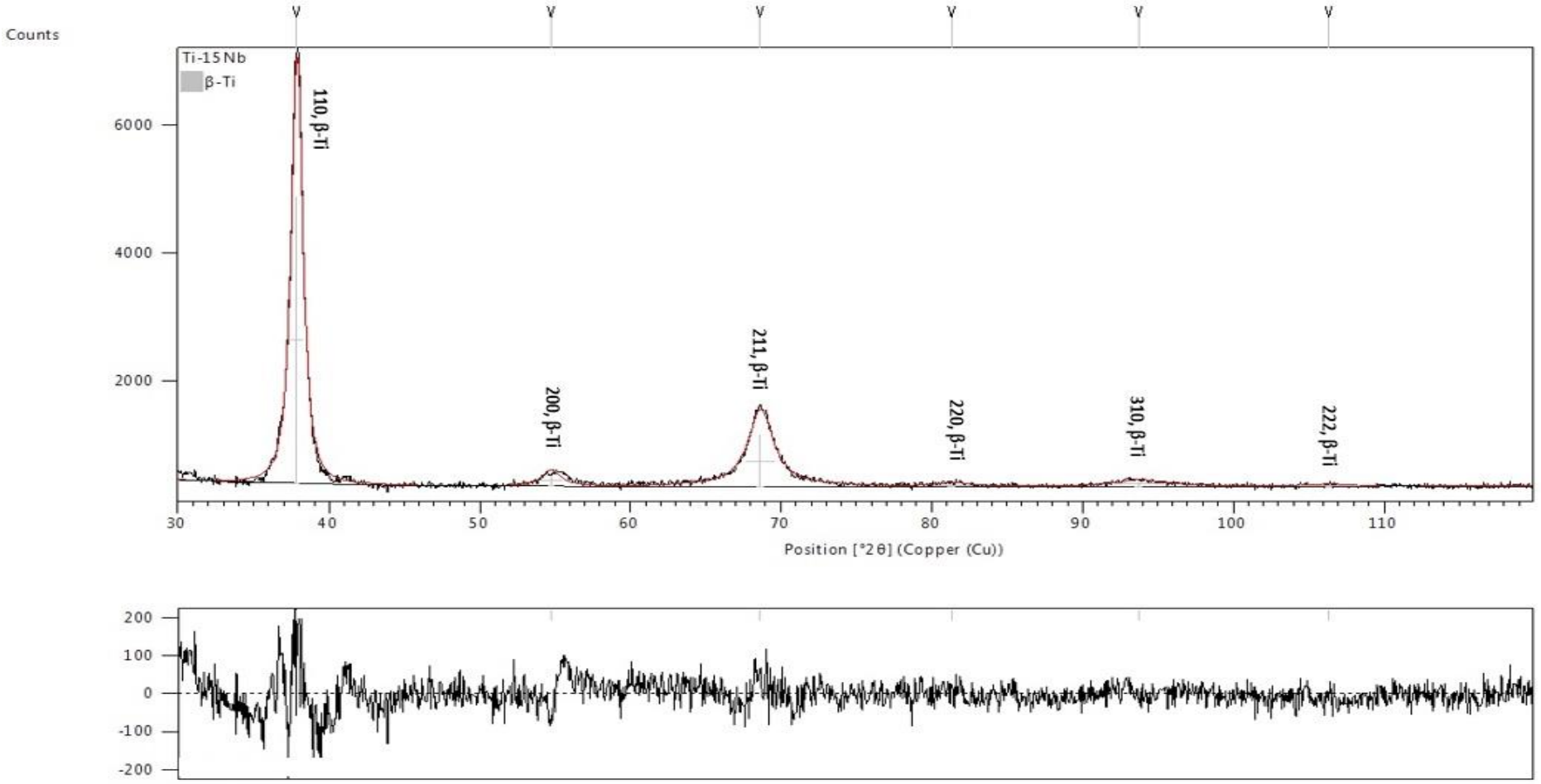

Figure 29: Observed and calculated profiles for the Pawley refinement of Ti-15Nb.The final agreement factors were R_p = 7.305%, R_{wp} = 8.081% and χ^2 = 0.940. The second graph is the difference plot.

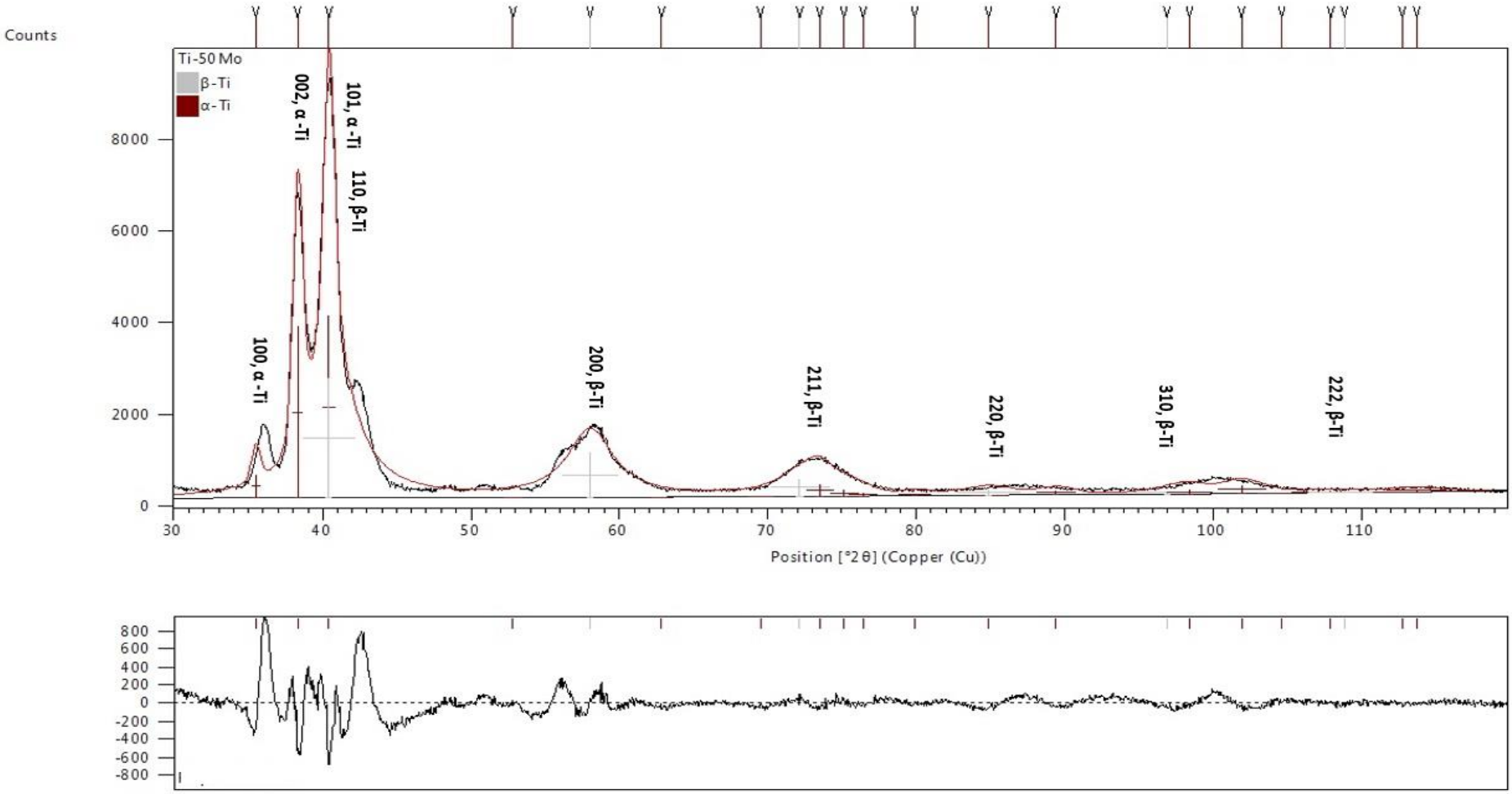

Figure 30: Observed and calculated profiles for the Pawley refinement of Ti-50Mo.The final agreement factors were R_p = 7.079%, R_{wp} = 9.159% and χ^2 = 2.597. The second graph is the difference plot.

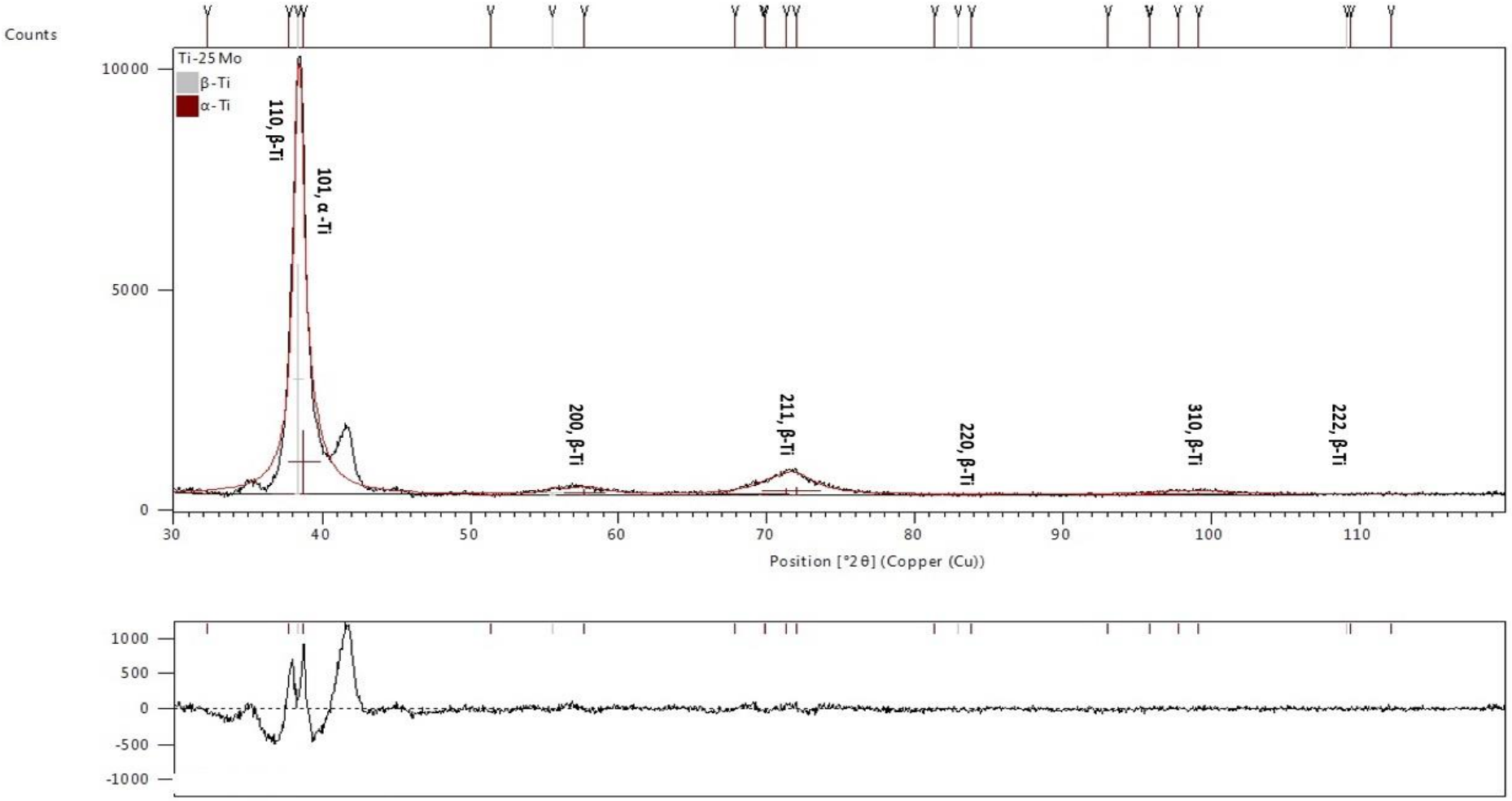

Figure 31: Observed and calculated profiles for the Pawley refinement of Ti-25Mo.The final agreement factors were R_p = 7.566%, R_{wp} = 8.808% and χ^2 = 1.260. The second graph is the difference plot.

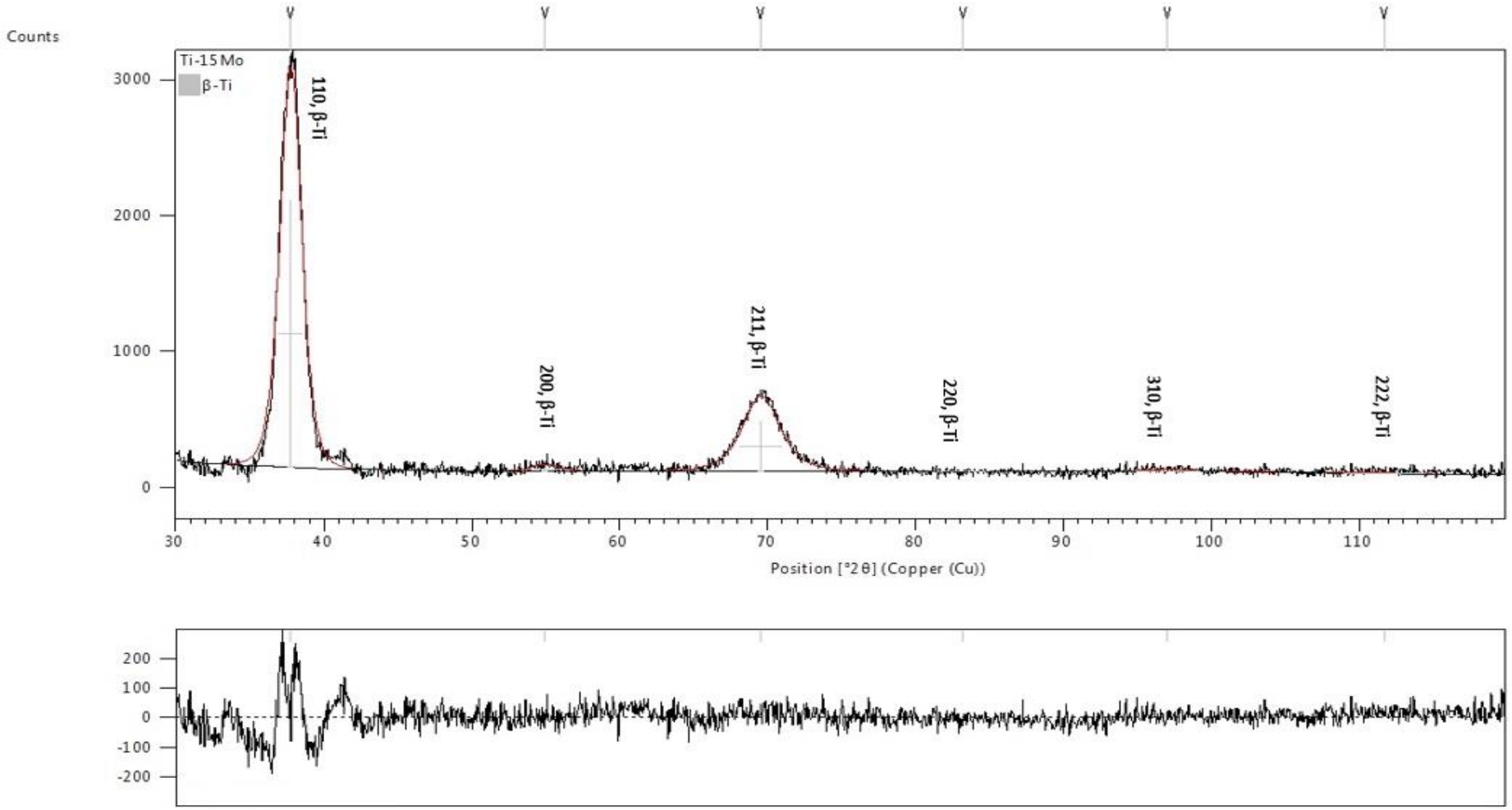

Figure 32: Observed and calculated profiles for the Pawley refinement of Ti-15Mo.The final agreement factors were R_p = 8.151%, R_{wp} = 9.316% and χ^2 = 0.990. The second graph is the difference plot.

Appendix B

Vacuum Pumps

Rotary Vane Pump

A rotary vane pump is an example of a roughing pump typically used. The pump follows a continuous four stage cycle through the rotation of two eccentrically mounted, spring loaded vanes. The enclosed system is thoroughly sealed and lubricated and depicted in Figure 33**Error! Reference source not found.**. The stages a re as follows:

Induction - The inlet port allows gas into the lower pump chamber.

Isolation – As the vane rotates, both the inlet and exhaust ports are isolated.

Compression – Further rotation compresses the gas.

Exhaust – Final rotation reveals the exhaust port, allowing the compressed gas to escape through a non-return valve.

Multiple systems in series can improve the efficiency of rotary vane pumps.

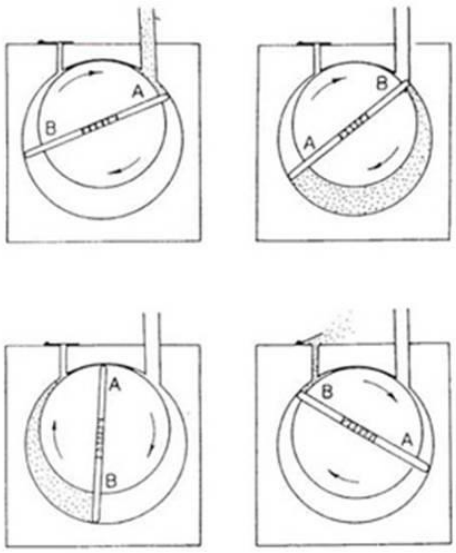

Figure 33: Schematic of the four stages of a Rotary Vane Pump (Egerton, 2005)

Diffusion Pump

A diffusion pump, illustrated in Figure 34, uses high speed jets of preheated vapour which when condensed on its cooled internal sides reduces the pressure in a chamber mounted above (Potts, 1987). In its simplest form there are no moving parts. Diffusion pumps are capable of reaching high-vacuums of ≈ 1 x 10^{-6} Pa, however must be used in conjunction with a roughing pump and backing pump to avoid damage caused by exposure to atmospheric pressure.

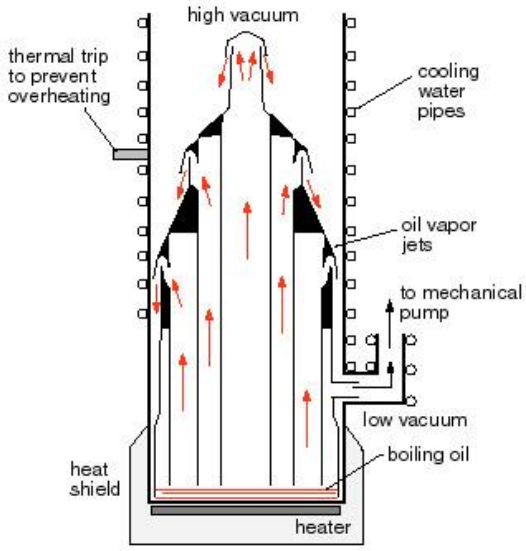

Figure 34: Schematic of a Diffusion Pump

Vacuum Measurement

Pirani Gauge

A Pirani gauge is a thermal conductivity gauge that uses a metal filament to measure the number of gas molecules present as they collide with it and exchange thermal energy.

The Pirani gauge was developed by Marcello Pirani in 1906 (Chambers, 2005). It is a thermal conductivity gauge that measures the number of molecules present by interpreting the variance in thermal energy when the molecules collide with the gauges metal filament. The thermal energy recognised has a direct effect on the resistance in the circuit, which can be measured and displayed as a pressure value

based on the number molecules. The gauge can be used from atmospheric pressure to ≈ 1 x 10^{-1} Pa, however must be calibrated based on the specific gas in question (Chambers, 2005).

Penning Gauge

The Penning Gauge, a type of cold-cathode ionisation gauge, was invented by Frans Penning in 1963 (Chambers, 2005). A discharge is maintained between two electrodes with a potential difference of 3kV. The electrons are forced into spiral paths by an axial magnetic field resulting in an increase in the ionisation current and sensitivity. The values obtained for ionisation current are converted into a pressure value using a suitable control unit. The gauge typically has an operating range between 1Pa and 1 x 10^{-7} Pa.

Baratron® Gauge

Baratron® is the trademark name for a capacitance manometer. The basic principle consists of a reference vacuum separated from the chamber vacuum by a metallic diaphragm; the displacement of the diaphragm, as a result of the difference in pressure, is measured electrically using a fixed dual electrode arrangement; the change in mutual capacitance, between the diaphragm and the electrode arrangement, is converted to a pressure reading. The gauge measures true pressure; therefore, it is not sensitive to the type of gas being measured. The most sensitive instruments can measure pressures in the range 1Pa - 1 x 10^{-3} Pa (Chambers, 2005).

References

13th Annual Report. (2016): National Joint Registry for England, Wales and Northern Ireland and the Isle of Man.

14th Annual Report. (2017): National Joint Registry for England, Wales and Northern Ireland and the Isle of Man.

15th Annual Report. (2018): National Joint Registry for England, Wales and Northern Ireland and the Isle of Man.

Achache, S., S. Lamri, Arab Pour Yazdi, M., Billard, A., François, M. and Sanchette, F. (2015) 'Ni-free superelastic binary Ti–Nb coatings obtained by DC magnetron co-sputtering.' *Surface & Coatings Technology*, 275 pp. 283–288.

Achache, S., Lamri, S., Alhussein, A., Billard, A., François, M. and Sanchette, F. (2016) 'Gum Metal thin films obtained by magnetron sputtering of a Ti-Nb-Zr- Ta target.' *Materials Science & Engineering A*, 673 pp. 492–502.

Adachi, H., Hata, T., Matsushima, T., Motohiro, T. and Tominaga, K. (2012*) Handbook of Sputter Deposition Technology.* Elsevier, USA.

Al-Nasiry, S., Geusens, N., Hanssens, M., Luyten, C. and Pijnenborg, R. (2007) 'The use of Alamar Blue assay for quantitative analysis of viability, migration and invasion of choriocarcinoma cells.' *Human Reproduction*, 22(5) pp. 1304–1309.

Allegheny Technologies Incorporated, ATI. (2014) 'ATI 15Mo™ Titanium Alloy: Technical Data Sheet.' Version 2.

Anjum, Z., Qayyum, F., Khushnood, S., Ahmed, S. and Shah, M. (2015) 'Prediction of non-propagating fretting fatigue cracks in Ti6Al4V sheet tested under pin-in-dovetail configuration: Experimentation and numerical simulation.' *Materials and Design*, 87 pp. 750–758.

Arthritis Research UK. (2011) 'Hip pain'.

Asri, R. I. M., Harun, W. S. W., Samykano, M., Lah, N. A. C., Ghani, S. A . C., Tarlochan, F. and Raza, M. R. (2017) 'Corrosion and surface modificationon biocompatible metals: A Review.' *Materials Science and Engineering C,* 77 pp. 1261-1274.

Bönisch, M., Calin, M., Waitz, T., Panigrahi, A., Zehetbauer, M., Gebert, A., Skrotzki, W. and Eckert, J. (2013) ‘ Thermal stability and phase transformations of martensitic Ti-Nb alloys.’ *Science and Technology of Advanced Materials,* 14.

Baker, H. (1992) ‘Introduction to Alloy Phase Diagrams.’ *ASM Handbook,* 3 pp. 1.1-1.29

Bates, R.I. and Arnell, R.D. (1997) ‘Microstructure of novel corrosion-resistant coatings for steel components by unbalanced magnetron sputtering.’ *Surface and Coatings Technology*, 89 pp. 204-212.

Beutner, R., Michael, J., Schwenzer, B. and Scharnweber, D. (2010) 'Biological nano-functionalization of titanium-based biomaterial surfaces: a flexible toolbox.' *Journal of The Royal Society Interface*, 7 pp. 93-105.

Birmingham, E., Niebur, G. L., McHugh, P. E., Shaw, G., Barry, F. P. and McNamara, L. M. (2012) 'Osteogenic differentiation of mesenchymal stem cells is regulated by osteocyte and osteblast cells in a simplified bone niche.' *European Cells and Materials*, 23 pp. 13-27.

Bobyn, J. D., Pilliar, R. M., Cameron, H. U. and Weatherly, G. C. (1980) ‘The optimum pore size for the fixation of porous surfaced metal implants by the ingrowth of bone.’ *Clin Orthop Relat Res*, 150 pp. 263-270.

Bockris, J. (2013) *Comprehensive treatise of electrochemistry.* Vol. 4. Electrochemical Materials Science. New York: Plenum Press.

Bondy, S. C. (2010) 'The neurotoxicity of environmental aluminum is still an issue.' *Neurotoxicology*, 31 pp. 575-581.

Bourn, J. (2003) *Hip replacements: an update.* London: National Audit Office.

Bozic, K. J., Kamath, A. F., Ong, K., Lau, E., Kurtz, S., Chan, V., Vail, T. P., Rubash, H. and Berry, D. J. (2015) ‘Comparative epidemiology of revision arthroplasty: failed THA poses greater clinical and economic burdens than failed TKA.’ *Clinical Orthopaedics and Related Research,* 473(6) pp. 2131–2138.

Brett, M. J., Tait, R. N., Dew, S. K., Kamasz, S. and Labun, A. H. (1992) ‘Nodular defect growth in thin films.’ *Journal of Materials Science: Materials in Electronics,* 3 pp. 64-70.

Browne , M. and Gregson , J. (1994) 'Surface modification of titanium alloy implants.' *Biomaterials*, 15(11) pp. 894-898.

Brune, H. (2001) ‘Growth modes.’ *Encyclopedia of Materials: Science and Technology*, pp. 3683–3693

Bönisch, M., Calin, M., Humbeeck, J. V., Skrotzki, W. and Eckert, J. (2015) 'Factors influencing the elastic moduli, reversible strains and hysteresis loops in martensitic Ti–Nb alloys.' *Materials Science and Engineering C*, 48 pp. 511-520.

Cao, W. and Hench, L. L. (1996) 'Bioactive Materials.' *Ceramics International*, 22 pp. 493-507.

Chambers, A. (2005) *Modern vacuum physics.* Betts, D. S. (ed.): Chapman & Hall.

Chang, L. L., Wang, Y. D. and Renc, Y. (2016) 'In-situ investigation of stress-induced martensitic transformation in Ti–Nb binary alloys with low Young's modulus.' *Materials Science & Engineering A*, 651 pp. 442–448.

Chen, J., Mwenifumbo, S., Langhammer, C., McGovern, J. P., Li, M., Beye, A. and Soboyejo, W. O. (2007) 'Cell/Surface Interactions and Adhesion on Ti-6Al-4V: Effects of Surface Texture.' *Journal of Biomedical Materials Research*, 82 pp. 360-373.

Chen, Q. and Thouas, G. A. (2015) 'Metallic implant biomaterials.' *Materials Science and Engineering R*, 87 pp. 1-57.

Chen, Y. Y., Xu, L. J., Liu, Z. G., Kong, F. T. and Chen, Z. Y. (2006) 'Microstructures and properties of titanium alloys Ti-Mo for dental use.' *Transactions of Nonferrous Metals Society of China,* 16 pp. 824-828.

Chiang, C., Chiou, S., Yang, W., Hsu, M., Yung, M., Tsai, M., Chen, L. and Huang, H. (2009) 'Formation of TiO2 nano-network on titanium surface increases the human cell growth.' *Dental Materials*, 25 pp. 1022–1029.

Correa, D. R. N., Vicente, F. B., Araujo, R. O., Lourenco, M. L., Kuroda, P. A. B., Buzalaf, M. A. R. and Grandini, C. R. (2015) 'Effect of the substitutional elements on the microstructure of the Ti-15Mo-Zr and Ti-15Zr-Mo systems alloys.' *Journal of Materials Research and Technology*, 4(2) pp. 180-185.

Crapper McLachlan, D.R., Lukiw, W.J. and Kruck, T.P.A. (1989) ‘New evidence for an active role aluminium in alzheimer’s disease.’ *The canadian journal of neurological sciences,* 16 pp. 490-497.

Cui, J., Qianga, L., Zhang, B., Linga, X., Yanga, T. and Zhang, J. (2012) 'Mechanical and tribological properties of Ti-DLC films with different Ti content by magnetron sputtering technique.' *Applied Surface Science*, 258 pp. 5025–5030.

Dai, S., Wang, Y., Chen, F., Yu, X. and Zhang, Y. (2013) 'Design of new biomedical titanium alloy based on d-electron alloy design theory and JMatPro software.' *Trans. Nonferrous Met. Soc. China*, 23 pp. 3027−3032.

Egerton, R. F. (2005) *Physical Principles of Electron Microscopy: An Introduction to TEM, SEM, and AEM.* Springer US.

Eggenhofer, E., Luk , F., Dahlke , M. H. and Hoogduijn , M. J. (2014) 'The life and fate of mesenchymal stem cells.' 5 p. 6.

Eisenbarth, E., Velten, D., Muller, M., Thull, R. and Breme, J. (2004) 'Biocompatibility of b-stabilizing elements of titanium alloys.' *Biomaterials*, 25 pp. 5705–5713.

Elmore, S. (2007) 'Apoptosis: A Review of Programmed Cell Death.' *Toxicol Pathol.*, 35(4) pp. 495–516.

Ennos, R. (2012) *Statistical and Data Handling Skills in Biology.* 3rd edition ed.: Pearson Education Limited.

Evans, S., Jones, E., Fox, P. and Sutcliffe, C. (2017) 'Analysis of variability in additive manufactured open cell porous structures.' *Proceedings of the Institution of Mechanical Engineers Parth-Journal of Engineering in Medicine*, 231 (6) pp. 534-546.

Freedman, Y. (2012) *University physics with modern physics.* Whilton, N. (ed.) 13th ed.: Jim Smith.

Gavrilov, A. (no date) «Motor Sichi» played half a million prostheses for hospitals. [Online] [Accessed on 6th November 2018] https://hyser.com.ua/economics/116958-motorovtsy-razygrali-polmilliona-na-protezy-dlya-bolnits/amp

Geetha, M., Singh, A. K., Asokamani, R. and Gogia, A. K. (2009) 'Ti based biomaterials, the ultimate choice for orthopaedic implants - A review.' *Progress in Materials Science*, 54 pp. 397-425.

Geetha, M., Singh, A. K., Muraleedharan, K., Gogia, A. K. and Asokamani, R. (2001) 'Effect of thermomechanical processing on microstructure of aTi–13Nb–13Zr alloy.' *Journal of Alloys and Compounds*, 329 pp. 264-271.

Giannini, M., Giannaccini, M., Sibillano, T., Giannini, C., Liu, D., Wang, Z., Bau, A., Dente, L., Cuschieri, A. and Raffa, V. (2014) 'Sheets of Vertically Aligned BaTiO3 Nanotubes Reduce Cell Proliferation but Not Viability of NIH-3T3 Cells.' *PLoS ONE*, 9(12) pp. 1-18.

Goriainov, V., Cook, R., Latham, J. M., Dunlop, D. G. and Oreffo, R. O. C. (2014) 'Bone and metal: An orthopaedic perspective on osseointegration.' *Acta Biomaterialia*, 10 pp. 4043-4057.

Hafner, B. 'Energy Dispersive Spectroscopy on the SEM: A Primer.' Characterization Facility, University of Minnesota.

Hallab, N. J. and Jacobs, J. J. (2017) 7.8 Implant Debris: Clinical Data and Relevance. In: *Comprehensive Biomaterials II*, 2nd ed. Elsevier, pp.118–132.

Han, M. K., Hwang, M. J., Yang, M. S., Yang, H. S., Song, H. J. and Park, Y. J. (2014) 'Effect of zirconium content on the microstructure, physical properties and corrosion behavior of Ti alloys.' *Materials Science and Engineering A*, 616 pp. 268-274.

Harrison, M. A. and Rae, I. F. (1997) *General techniques of cell culture.* Handbooks in Practical Animal Cell Biology. Cambridge: Cambridge University Press.

Hay, G. A. (1982) *Traditional x-ray imaging. .* Scientific basis of medical imaging.

Heimann, R. B. (2006) 'Thermal spraying of biomaterials.' *Surface & Coatings Technology*, 201 pp. 2012–2019.

Hermawan, H., Ramdan, D. and Djuansjah, J. R. P. (2011) 'Metals for Biomedical Applications.' *In* Fazel, P. R. (ed.) *Biomedical Engineering - From Theory to Applications*. InTech.

Hickman, B. S. (1969) 'The formation of omega phase in titanium and zirconium alloys: A review.' *Journal of Materials Science,* 4(6) pp.554-563.

Ho, W. F., Ju, C. P. and Chern Lin, J. H. (1999) 'Structure and properties of cast binary Ti-Mo alloys.' *Biomaterials*, 20 pp. 2115-2122.

Hon, Y., Wang, J. and Pan, Y. (2003) 'Composition/phase structure and properties of Titanium-Niobium alloys.' *Materials Transactions*, 44(11) pp. 2384-2390.

Huggler, A. H. and Weidmann, E. (1976) 'Design Criteria of Total Hip Replacements Fixed with Bone Cement.' *In* Schaldach , M. and Hohmann , D. (eds.) *Engineering in Medicine*. Vol. Volume 2: Advances in Artificial Hip and Knee Joint Technology. Springer Berlin Heidelberg, pp. 361-373.

Jones, E., Sutcliffe, C., and Stamp, R. (2007) 'Laser-produced porous surface.' Patent no. EP1683593.

Karp, G. (2014) *Cell Biology.* Singapore: John Wiley & Sons.

Karre, R., Niranjan, M. K. and Dey, S. R. (2015) 'First principles theoretical investigations of low Young's modulus beta Ti–Nb and Ti–Nb–Zr alloys compositions for biomedical applications.' *Materials Science and Engineering C*, 50 pp. 54-58.

Kelly, P. J. (1997) *Characterization studies of a closed-field unbalanced magnetron sputtering system.* PhD. University of Salford.

Kienapfel, H., Sprey, C., Wilke, A. and Griss, P. (1999) 'Implant fixation by bone ingrowth.' *J Arthroplasty*, 14 pp. 355-368.

Kim, Y. and Choi, H. Y. (2017) 'Characterization of Ti/W, Ti/Cr, and Ti/Pt thin films−part I: Surface morphologies and nano-mechanical properties.' *Sensors and Actuators A: Physical*, 254 pp. 9–19.

Kolli, R. P. and Devaraj, A. (2018) 'A review of metastable beta titanium alloys.' *Metals,* 8(506).

Kokubo, T., Kim, H. and Kawashita, M. (2003) 'Novel bioactive materials with different mechanical properties.' *Biomaterials*, 24 pp. 2161–2175.

Kopova, I., Stráský, J., Harcuba, P., Landa, M., Janeček, M. and Bačákova, L. (2016) 'Newly developed Ti–Nb–Zr–Ta–Si–Fe biomedical beta titanium alloys with increased strength and enhanced biocompatibility.' *Materials Science and Engineering C*, 60 pp. 230–238.

Kuroda, P. A. B., Buzalaf, M. A. and Grandini, C. R. (2016) 'Effect of molybdenum on structure, microstructure and mechanical properties of biomedical Ti-20Zr-Mo alloys.' *Materials Science and Engineering*, 67 pp. 511-515.

Lee, Y. E. and Lee, J. B. (1996) Microstructural evolution and preferred orientation change of radio-frequency-magnetron sputtered ZnO thin films.' *Journal of Vacuum Science and Technology A,* 14.

Li, S., Chow, T. and Chu, J. (2017) 'Engineering microdent structures of bone implant surfaces to enhance osteogenic activity in MSCs.' *Biochemistry and Biophysics Reports*, 9 pp. 100–105.

Li, Y., Yang, C., Zhao, H., Qu, S., Li, X. and Li, Y. (2014) 'New Developments of Ti-Based Alloys for Biomedical Applications.' *Materials*, 7 pp. 1709-1800.

Liang, S. X., Feng, X. J., Yin, L. X., Liu, X. Y., Ma, M. Z. and Liu, R. P. (2016) 'Development of a new beta Ti alloy with low modulus and favorable plasticity for implant material.' *Materials Science and Engineering C*, 61 pp. 338-343.

Lin, C. W., Ju, C. P. and Chern Lin, J. H. (2005) 'A comparison of the fatigue behavior of cast Ti–7.5Mo with c.p. titanium, Ti–6Al–4V and Ti–13Nb–13Zr alloys.' *Biomaterials*, 26 pp. 2899–2907.

Lincks, J., Boyan, B. D., Blanchard, C. R., Lohmann, C. H., Liu, Y., Cochran, D. L., Dean, D. D. and Schwartz, Z. (1998) 'Response of MG63 osteoblast-like cells to titanium and titanium alloy is dependent on surface roughness and composition.' *Biomaterials*, 19 p. 2219—2232.

Liu, X., Chu, P. K. and Ding, C. (2004) 'Surface modification of titanium, titanium alloys, and related materials for biomedical applications.' *Materials Science and Engineering R*, 47 pp. 49–121.

Liu, G., Yang, Y., Jin, N., Luo, X., Huang, B., Li, P. and Kou, Z. (2018) 'The structural characterisations of Ti-17 alloy films prepared by magnetron sputtering.' *Applied Surface Science,* 427 pp. 774-781.

Long, M. and Rack, H. J. (1998) 'Titanium alloys in total joint replacement—a materials science perspective.' *Biomaterials*, 19 pp. 1621-1639.

Lopes, E. S. N., Contieri, R. J., Button, S. T. and Caram, R. (2015) 'Femoral hip stem prosthesis made of graded elastic modulus metastable beta Ti alloy.' *Materials and Design*, 69 pp. 30-36.

Lord, M. S., Modin, C., Foss, M., Duch, M., Simmons, A., Pedersen, F. S., Milthorpe, B. K. and Besenbacher, F. (2006) 'Monitoring cell adhesion on tantalum and oxidised polystyrene using a quartz crystal microbalance with dissipation.' *Biomaterials*, 27(26) pp. 4529-4537.

Marker, C., Shang, S. L., Zhao, J. C. and Liu, Z. K. (2018). 'Effects of alloying elements on the elastic properties of bcc Ti-X alloys from first-principles calculations.' *Computational Materials Science*, 142 pp. 215–226.

Martin, J. Y., Schwartz, Z., Hummert, T. W., Schraub, D. M., Simpson, J., Lankford, J., Dean, D. D., Cochran, D. L. and Boyan, B. D. (1995) 'Effect of titanium surface roughness on proliferation, differentiation, and protein synthesis of human osteoblast-like cells (MG63).' *Journal of Biomedical Materials Research*, 29 pp. 389-401.

Masahashi, N., Mizukoshi, Y., Semboshi, S., Ohmura, K. and Hanada, S. (2012) 'Photo-induced properties of anodic oxide films on Ti6Al4V.' *Thin Solid Films*, 520 pp. 4956–4964.

Matsumoto, H., Watanabe, S. and Hanada, S. (2005) 'Beta TiNbSn Alloys with Low Young's Modulus and High Strength.' *Materials Transactions*, 46(5) pp. 1070-1078.

Medda , R., Helth , A., Herre , P., Pohl , D., Rellinghaus , B., Perschmann , N., Neubauer , S., Kessler , H., Oswald , S., Eckert , J., Spatz , J. P., Gebert , A. and Cavalcanti-Adam , E. A. (2014) 'Investigation of early cell–surface interactions of human mesenchymal stem cells on nanopatterned b-type titanium–niobium alloy surfaces.' *Interface Focus*, 4(1).

Milosev, I., Metikos-Hukovic, M. and Strehblow, H. (2000) 'Passive film on orthopaedic TiAlV alloy formed in physiological solution investigated by X-ray photoelectron spectroscopy.' *Biomaterials*, 21(20) pp. 2103-2113.

Mohseni, E., Zalnezhad, E. and Bushroa, A. R. (2014) 'Comparative investigation on the adhesion of hydroxyapatite coating on Ti-6Al-4V implant: A review paper.' *International Journal of Adhesion & Adhesives*, 48 pp. 238-257.

Morgado, T. L. M., Navas, H. and Brites, R. (2016) 'Wear study of innovative Ti-Ta alloys.' *Procedia S tructural Integrity,* 2 pp. 1266-1276.

Mullen, L., Stamp, R. C., Brooks, W. K., Jones, E. and Sutcliffe, C. J. (2009) 'Selective Laser Melting: A regular unit cell approach for the manufacture of porous, titanium, bone in-growth constructs, suitable for orthopedic applications.' *Journal of Biomedical Materials Research Part B: Applied Biomaterials*, 89B(2) pp. 325-334.

Murray, J.L. (1987) 'Phase diagrams of binary titanium alloys.' *ASM International*, pp. 169-345.

Musil, J. and Bell, J. (1996) 'Formation of high temperature phases in sputter deposited Ti-based films below 100°C.' *Journal of Vacuum Science and Technology,* 14(4) pp. 2247-2250.

Ng, F. Y., Zhang, J. T., Chui, K. Y. and Yan, C. H. (2011) 'A cadaveric study of posterior dislocation after total hip replacement-effects of head diameter and acetabular anteversion.' International Orthopedics, 35 (3), pp. 325-329.

Niinomi, M., Nakai, M. and Hieda, J. (2012) 'Development of new metallic alloys for biomedical applications.' *Acta Biomaterialia*, 8 pp. 3888–3903.

Ogura, N., Kawada, M., Change, W.-J., Zhang, Q., Lee, S.-Y., Kondoh, T. and Abiko, Y. (2004) 'Differentiation of the human mesenchymal stem cells derived from bone marrow and enhancement of cell attachment by fibronectin.' *Journal of Oral Science*, 46(4) pp. 207-213.

Ohring, H. (1991) 'The materials science of thin films.' *Academic Press*, London.

Ojha, A. and Sehitoglu, H. (2016) 'Critical stress for the bcc–hcp martensite nucleation in Ti–6.25at.%Ta and Ti–6.25at.%Nb alloys.' *Computational Materials Science*, 111 pp. 157-162.

Oliveira, I. R., Andrade, T. L., Araujo, K. C. M. L., Luz, A. P. and Pandolfelli, V. C. (2016) 'Hydroxyapatite synthesis and the benefits of its blend with calcium aluminate cement.' *Ceramics International*, 42 pp. 2542–2549.

Oliveira, N. and Guastaldi, A. (2006) 'Electrochemical studies on Ti-Mo alloys of interest to biomaterials.' *Corrosão e Protecção de Materiais*, 26(2)

Oliveira, N. T. C., Aleixo, G., Caram, R. and Guastaldi, A. C. (2007) 'Development of Ti–Mo alloys for biomedical applications: Microstructure and electrochemical characterization.' *Materials Science and Engineering A*, pp. 727–731.

PANalytical. (2014) *X'Pert³ Powder.*

Park, J. and Lakes, R. S. (2010) *Biomaterials, an introduction.* 3 ed.: Springer.

Potts, P. J. (1987) *A handbook of silicate rock analysis.* Blackie.

Quiroz, F. G., Posada Estefan, O. M., Gallego Pérez, D., Higuita Castro, N., Sarassa V elásquez, C. A., Hansford, D. J., Agudelo Florez, P. and López Rojas, L. E. (2008) 'Isolation of human bone marrow mesenchymal stem cells and evaluation of their osteogenic potential.' *Revista Ingeniería Biomédica*, 2 pp. 48-55.

Rack, H. J. and Qazi, J. I. (2006) 'Titanium alloys for biomedical applications.' *Materials Science and Engineering C*, 26 pp. 1269 – 1277.

Ratova, M. (2013) *Enhanced properties of photocatalytic titania thin films via doping during magnetron sputter deposition.* PhD. Manchester Metropolitan University.

Ratova, M., Klaysria, R., Praserthdam, P. and Kelly, P. J. (2017a) 'Pulsed DC magnetron sputtering deposition of crystalline photocatalytic titania coatings at elevated process pressures.' *Materials Science in Semiconductor Processing*, 71 pp. 188-196.

Ratova, M., Kelly, P. J., West, G. T., Tosheva, L. and Edge, M. (2017b) 'Reactive magnetron sputtering deposition of bismuth tungstate onto titania nanoparticles for enhancing visible light photocatalytic activity.' *Applied Surface Science*, 392 pp. 590–597.

Ridzwan, M. I. Z., Shuib, S., Hassan, A. Y., Shokri, A. A. and Mohamad Ibrahim, M. N. (2007) 'Problem of Stress Shielding and Improvement to the Hip Implant Designs: A Review.' *Journal of Medical Sciences*, 7 pp. *460-467*.

Rosa, A. L. and Beloti, M. M. (2003) 'Effect of cpTi Surface Roughness on Human Bone Marrow Cell Attachment, Proliferation, and Differentiation.' *Brazilian Dental Journal*, 14(1) pp. 16-21.

Saito, T., Furuta, T., Hwang, J. H., Kuramoto, S., Nishino, K., Suzuki, N., Chen, R., Yamada, A., Ito, K., Seno, Y., Nonaka, T., Ikehata, H., Nagasako, N., Iwamoto, C., Ikuhara, Y. and Sakuma, T. (2003) 'Multifunctional Alloys Obtained via a Dislocation-Free Plastic Deformation Mechanism .' *Science*, 300 pp. 464-467.

Santiago-Medina, P., Sundaram, P. A. and Diffoot-Carlo, N. (2014) 'The Effects Of Micro Arc Oxidation Of Gamma Titanium Aluminide Surfaces On Osteoblast Adhesion And Differentiation.' *Journal of Materials Science: Materials in Medicine*, 25(6) pp. 1577–1587.

Santiago-Medina, P., Sundaram, P. A. and Diffoot-Carlo, N. (2015) 'Titanium Oxide: A Bioactive Factor in Osteoblast Differentiation.' *International Journal of Dentistry*,

Satoh, K., Ohtsu, N., Sato, S. and Wagatsuma, K. (2013) 'Surface modification of Ti–6Al–4V alloy using an oxygen glow-discharge plasma to suppress the elution of toxic elements into physiological environment.' *Surface & Coatings Technology*, 232 pp. 298–302.

Satoh, K., Komata, M., Mizuhira, M., Wagatsuma, K. and Ohtsu, N. (2013) 'Direct and Rapid Quantification of Calcium Phosphate Precipitate on Titanium by X-Ray Fluorescence Analysis Using Fundamental Parameter Method.' *Materials Transactions*, 54(5) pp. 817-824.

Sawyer, A. A., Hennessy, K. M. and Bellis, S. L. (2007) 'The effect of adsorbed serum proteins, RGD and proteoglycan-binding peptides on the adhesion of mesenchymal stem cells to hydroxyapatite.' *Biomaterials*, 28 pp. 383-392.

Semlitsch, M. (1987) 'Titanium alloys for hip joint replacements.' *Clinical Materials*, 2(1) pp. 1-13.

Sharma, B., Vajpai, S. K. and Ameyama, K. (2016) 'Microstructure and properties of beta Ti–Nb alloy prepared by powder metallurgy route using titanium hydride powder.' *Journal of Alloys and Compounds*, 656 pp. 978-986.

Shi, J. D., Wu, K. H. and Larkins, G. (1997) 'A Method for Measuring the Elastic Modulus of Thin Films.' *Materials Characterization*, 38 pp. 301-303.

Silva, H. M., Schneider, S. G. and Moura Neto, C. (2004) 'Study of nontoxic aluminum and vanadium-free titanium alloysfor biomedical applications.' *Materials Science and Engineering C*, 24 pp. 679-682.

Simoneau, C., Terriault, P., Jetté, B., Dumas, M. and Brailovski, V. (2017) 'Development of a porous metallic femoral stem: Design, manufacturing, simulation and mechanical testing.' *Materials and Design*, 114 pp. 546–556.

Sing Ng, B., Annergren, I., Soutar, A. M., Khor, K. A. and Jarfors, A. E. W. (2005) 'Characterisation of a duplex TiO 2 /CaP coating on Ti6Al4V for hard tissue replacement.' *Biomaterials*, 26(10) pp. 1087-1095.

Slack, J. (2012) *Stem Cells: A Very Short Introduction.* United States: Oxford University Press.

Song, G. (2005) 'Transpassivation of Fe–Cr–Ni stainless steels.' *Corrosion Science*, 47(8) pp. 1953–1987.

Structure Determination from Powder Diffraction Data. (2006) New York: Oxford University Press.

Sullivan, M., Galea, P. and Latif, S. (2006) 'What is the appropriate oxygen tension for *in vitro* culture?' MHR: Basic science of reproductive medicine. 12(11) p. 653.

Thornton, J. A. (1974) Journal of Vacuum Science & Technology , 11, pp. 666.

Todaro, G. J. and Green, H. (1963) 'Quantitative studies of the growth of mouse embryo cells in culture and their development into established lines.' *J Cell Biol.* 17(2) pp. 299-313.

Trinkle, D. R. (2003) *A theoretical study of the HCP to Omega martensitic phase transition in Titanium.* PhD. The Ohio State University.

Ullah, I., Subbarao, R. B. and Rho, G. J. (2015) 'Human mesenchymal stem cells- current trends and future propective.' *Bioscience Reports*, 35 pp. 1-18.

Wang, M. (2003) 'Developing bioactive composite materials for tissue replacement.' *Biomaterials*, 24 pp. 2133-2151.

Wei, Q., Wang, Y., Li, X., Yang, M., Chai, W., Wang, K. and Zhang, Y. (2016) 'Study the bonding mechanism of binders on hydroxyapatite surface and mechanical properties for 3DP fabrication bone scaffolds.' *Journal of the mechanical behavior of biomedical materials*, 57 pp. 190-200.

Wei, X., Yang , X., Han , Z. P., Qu, F. F., Shao , L. and Shi , Y. F. (2013) 'Mesenchymal stem cells: a new trend for cell therapy.' *Acta Pharmacologica Sinica*, 34 pp. 747-754.

Williams, D. F. (2008) 'On the mechanisms of biocompatibility.' *Biomaterials*, 29(20) pp. 2941-2953.

Whiteside, P. J. D., Chininis, J. A. and Hunt, K. A. (2016) 'Techniques and Challenges for Characterizing Metal Thin Films with Applications in Photonics.' *Coatings,* 6 (35).

Wu, C. Y., Xin, Y. H., Wang, X. F. and Lin, J. G. (2010) 'Effects of Ta content on the phase stability and elastic properties of beta Ti-Ta alloys from first-principles calculations.' *Solid State Sciences*, 12 pp. 2120-2124.

Yan, W., Berthe, J. and Wenc, C. (2011) 'Numerical investigation of the effect of porous titanium femoral prosthesis on bone remodeling.' *Materials and Design*, 32 pp. 1776–1782.

Yang, W. and Huang, H. (2010) 'Improving the biocompatibility of titanium surface through formation of a TiO2 nano-mesh layer.' *Thin Solid Films*, 518 pp. 7545–7550.

You, L. and Song, X. (2012) 'A study of low Young's modulus Ti–Nb–Zr alloys using d electrons alloy theory.' *Scripta Materialia*, 67 pp. 57-60.

Zhang, Y., Khan , D., Delling , J. and Tobiasch , E. (2011) 'Mechanisms underlying the osteo- and adipo- differentiation of human mesenchymal stem cells.' *The Scientific World Journal*, p. 14.

Zhao, D., Chang, K., Ebel, T., Nie, H., Willumeit, R. and Pyczak, F. (2015) 'Sintering behavior and mechanical properties of a metal injection molded Ti–Nb binary alloy as biomaterial.' *Journal of Alloys and Compounds*, 640 pp. 393-400.

Zhou, Y. L., Niinomi, M. and Akahori, T. (2004) 'Effects of Ta content on Young's modulus and tensile properties of binary Ti–Ta alloys for biomedical applications.' *Materials Science and Engineering A*, 371 pp. 283–290.

Zhou, Y. L., Niinomi, M., Akahori, T., Fukui, H. and Toda, H. (2005) 'Corrosion resistance and biocompatibility of Ti–Ta alloys for biomedical applications.' *Materials Science and Engineering A*, 398 pp. 28-36.